

## MIT Open Access Articles

*Targeted Magnetic Nanoparticles for Remote  
Magnetothermal Disruption of Amyloid- $\beta$  Aggregates*

The MIT Faculty has made this article openly available. **Please share**  
how this access benefits you. Your story matters.

**Citation:** Loynachan, Colleen N., Gabriela Romero, Michael G. Christiansen, Ritchie Chen, Rachel Ellison, Tiernan T. O'Malley, Ulrich P. Froriep, Dominic M. Walsh, and Polina Anikeeva. "Targeted Magnetic Nanoparticles for Remote Magnetothermal Disruption of Amyloid- $\beta$  Aggregates." *Adv. Healthcare Mater.* 4, no. 14 (August 19, 2015): 2100–2109.

**As Published:** <http://dx.doi.org/10.1002/adhm.201500487>

**Publisher:** John Wiley & Sons

**Persistent URL:** <http://hdl.handle.net/1721.1/103060>

**Version:** Author's final manuscript: final author's manuscript post peer review, without publisher's formatting or copy editing

**Terms of use:** Creative Commons Attribution-Noncommercial-Share Alike



DOI: 10.1002/ ((please add manuscript number))

**Article type: Full Paper**

**Title** Targeted Magnetic Nanoparticles for Remote Magnetothermal Disruption of Amyloid- $\beta$  Aggregates

*Colleen N. Loynachan,<sup>†1</sup> Gabriela Romero,<sup>†2</sup> Michael G. Christiansen,<sup>†1</sup> Ritchie Chen,<sup>1</sup> Rachel Ellison,<sup>1</sup> Tiernan T. O'Malley,<sup>3</sup> Ulrich P. Froriep,<sup>2</sup> Dominic M. Walsh,<sup>3</sup> and Polina Anikeeva<sup>1,2\*</sup>*

C. Loynachan, M. Christiansen, R. Chen, R. Ellison, P. Anikeeva  
Department of Materials Science and Engineering  
Massachusetts Institute of Technology  
Cambridge, MA 02139, USA  
E-mail: anikeeva@mit.edu

G. Romero, U. Froriep, P. Anikeeva  
Research Laboratory of Electronics  
Massachusetts Institute of Technology  
Cambridge, MA 02139, USA

T. O'Malley, D. Walsh  
Laboratory for Neurodegenerative Research, Center for Neurologic Diseases  
Brigham and Women's Hospital and Harvard Medical School  
Boston, MA 02115, USA

<sup>†</sup> - These authors have contributed equally

**Keywords:** Magnetic nanoparticles, amyloid beta, disaggregation, magnetic hyperthermia

Remotely triggered hysteretic heat dissipation by magnetic nanoparticles (MNPs) selectively attached to targeted proteins can be used to break up self-assembled aggregates. We applied this magnetothermal approach to the amyloid- $\beta$  (A $\beta$ ) protein, which forms dense, insoluble plaques characteristic of Alzheimer's disease. Specific targeting of dilute MNPs to A $\beta$  aggregates was confirmed *via* transmission electron microscopy (TEM) and was found to be consistent with a statistical model of MNP distribution on the A $\beta$  substrates. MNP composition and size were selected to achieve efficient hysteretic power dissipation at physiologically safe alternating magnetic field (AMF) conditions. Dynamic light scattering, fluorescence spectroscopy, and TEM were used to characterize the morphology and size distribution of aggregates before and after exposure to AMF. We found a dramatic reduction

in aggregate size from microns to tens of nanometers, suggesting that exposure to an AMF effectively destabilizes A $\beta$  deposits decorated with targeted MNPs. Experiments in primary hippocampal neuronal cultures indicated that the magnetothermal disruption of aggregates reduced A $\beta$  cytotoxicity, which may enable future applications of this approach for studies of protein disaggregation in physiological environments.

## 1. Introduction

The aggregation of proteins such as amyloid beta (A $\beta$ ), prion, and  $\alpha$ -synuclein is the hallmark of over forty major human diseases.<sup>[1]</sup> These range from neurodegenerative conditions, such as Alzheimer's (AD) and Parkinson's disease, to non-neuropathic disorders, such as Type II diabetes and cardiac amyloidosis.

In an AD brain, the monomer of A $\beta$ , a 42 amino acid peptide sequence (A $\beta$ <sub>(1-42)</sub> ~ 4.5 kDa), which is unstructured in solution, nucleates and grows to form insoluble fibrils with a characteristic cross- $\beta$ -sheet structure. Fibrils then coalesce to form dense amyloid plaques bound by hydrogen bonds and hydrophobic interactions between the  $\beta$ -sheet structures.<sup>[2,3]</sup> Although the mechanisms of AD pathogenesis are not fully understood, it is hypothesized that clearance of A $\beta$  aggregates can result in cognitive improvement and reverse the progression of the disease.<sup>[4-6]</sup> Recently, soluble forms of A $\beta$  protein oligomers rather than aggregates have been implicated in AD pathology.<sup>[7-10]</sup> Thus, precise, minimally-invasive control of A $\beta$  aggregation state may enable basic studies of the role of this peptide in AD pathogenesis.

$\beta$ -sheet breaker peptides and nanoparticles have been investigated as laboratory tools to disrupt fibril and aggregate formation. The former can hinder A $\beta$  aggregation at high concentrations, though with limited efficacy due to insufficient steric hindrance.<sup>[11,12]</sup> Similarly, nanoparticles can prevent amyloid aggregation via protein adsorption on their surface.<sup>[13]</sup> However, the mechanism of this passive inhibition is not well understood, and depending on their concentration and surface chemistry, nanoparticles may instead accelerate

protein aggregation.<sup>[14]</sup> Local heating of gold and graphene oxide nanoparticles in the presence of microwave and near infrared electromagnetic waves has been suggested as a means to disaggregate amyloid deposits.<sup>[15–19]</sup> However, noninvasive delivery of NIR and microwave radiation deep into the brain at the required intensities may limit the feasibility of these approaches, due to scattering and absorption by several centimeters of skin, skull, dura matter.<sup>[20,21]</sup>

In this article, we present a method to remotely disaggregate A $\beta$  deposits using the local heat dissipated by magnetic nanoparticles (MNPs) in the presence of an alternating magnetic field (AMF) (**Figure 1**). Due to the low conductivity and magnetic susceptibility of biological matter, AMFs with frequencies ranging 10 kHz–10 MHz penetrate deep into body with negligible attenuation,<sup>[22]</sup> while avoiding damage to healthy tissue surrounding the aggregates. We hypothesized that AMF-induced heating of targeted MNPs is sufficient to disrupt the hydrophobic interactions and hydrogen bonds between fibrils and effectively destabilize the aggregates. To investigate the efficacy of the magnetothermal approach, we first chose MNPs that exhibit efficient heat dissipation at biomedically safe AMF conditions. Next, we engineered the surface of these MNPs to stabilize them in physiological fluids and chemically target A $\beta$ . We observed moderate clustering of MNPs on A $\beta$  aggregates from transmission electron microscopy (TEM) analysis, strongly suggesting the influence of magnetic interactions between MNPs during binding. This hypothesis was supported by a statistical model of interacting magnetic dipoles, which predicts similar behavior. The effect of the AMF exposure on A $\beta$  aggregates was quantified using fluorescence spectroscopy, dynamic light scattering (DLS) and TEM. Finally, we examined the biocompatibility of our magnetothermal approach on hippocampal neurons *in vitro*.

## 2. Results and Discussion

### 2.1. A $\beta$ Aggregation Process

We monitored A $\beta$  aggregation kinetics for 168 hrs at physiological conditions using thioflavin T (ThT) as an indicator of  $\beta$ -sheet fibril content.<sup>[23–25]</sup> Over the course of A $\beta$  aggregation (**Figure 2A**), ThT fluorescence profile exhibited an elongation phase followed by a plateau phase,<sup>[26]</sup> corresponding to the self-assembly and elongation of mature fibrils with a characteristic  $\beta$ -sheet structure (Figure 2B and S1). Our A $\beta$  samples showed a ThT fluorescence plateau at 24 hrs. In order to further examine the first 24 hrs of A $\beta$  aggregation, we employed DLS to measure the distribution of hydrodynamic radii ( $R_H$ ) of aggregates in solution (Figure 2C) without influencing the sample.<sup>[27]</sup> A 12 hr incubation time (corresponding to the aggregates  $R_H = 1.1 \pm 0.307 \mu\text{m}$ ) was chosen for the initial disaggregation experiments with MNPs and AMF to ensure that the 5  $\mu\text{m}$  upper detection limit of DLS did not skew the results.

## 2.2. Measurement of Hysteretic Heating of MNPs

For the proposed AMF-induced disaggregation of A $\beta$ , highly monodisperse and uniform MNPs were synthesized following our previous work.<sup>[28]</sup> The safety and biocompatibility of iron oxide based MNPs have already been established for diagnostic and therapeutic applications in the central nervous system, such as in magnetic resonance imaging, cancer hyperthermia, and drug delivery.<sup>[29–32]</sup> We reasoned that higher AMF-induced MNP power dissipation rate per gram of magnetic material, or specific loss power (SLP), would produce more effective disaggregation of A $\beta$  deposits. Nonspecific heating of healthy tissue via eddy currents induced by the applied AMF limits the product of the frequency  $f$  and the amplitude  $H_o$  of therapeutically acceptable AMFs to  $\leq 5 \times 10^9 \text{ Am}^{-1}\text{s}^{-1}$ .<sup>[33]</sup> To satisfy this condition and to perform experiments over the course of hours while maintaining the sample at  $37 \pm 2^\circ\text{C}$  with heat from the resistive losses of the coil, we used AMF with  $f = 100 \text{ kHz}$  and  $H_o = 28 \text{ kA/m}$ . At these AMF conditions, a SLP of 340 W/g(Fe) was observed for 22 nm Fe<sub>3</sub>O<sub>4</sub> particles. In

all samples containing MNPs, the concentration was 0.028mg Fe/mL, a value sufficiently low that no measureable bulk heating of the sample relative to control samples was observed.

### 2.3. Targeting MNPs to A $\beta$

Because polyethylene glycol (PEG) coatings stabilize MNPs in physiological fluids and impart an additional biocompatibility to the system for applications in neuronal cultures,<sup>[34]</sup> carbodiimide chemistry was used to graft 10 kDa PEG chains onto the poly(acrylic acid) (PAA)-passivated water soluble MNPs. In order to ensure close proximity during AMF application, MNPs must be specifically targeted to A $\beta$  aggregates. To this end, the carboxymethyl end group of the PEG-coated MNPs was functionalized with the peptide sequence leucine-proline-phenylalanine-phenylalanine-aspartic acid (LPFFD) (**Figure 3A**, estimation for degree of MNP functionalization in Figure S2), which binds to a hydrophobic domain on the A $\beta$  structure (amino acids 17-20).<sup>[11,15]</sup> While LPFFD peptide is a  $\beta$ -sheet breaker that can block A $\beta$  fibril growth and cause disaggregation in >10-fold molar excess with respect to A $\beta$  for extended incubation periods,<sup>[11,12,35]</sup> in this study, the ratio of LPFFD:A $\beta$  (1:15, with the unlikely assumption of 100% conversion) is far too low to inhibit fibril growth.<sup>[11]</sup> Structural studies indicate that the hydrophobic domain is largely confined to the fibril core,<sup>[36,37]</sup> which should restrict targeting to hydrophobic moieties exposed on the periphery of aggregates. The functionalization of MNPs was confirmed by measuring surface charge density (Figure 3B). PAA coated MNPs display a negative zeta potential of  $\sim -35$  mV and the zeta potential value increases to neutral values following PEG and LPFFD grafting, indicating the consumption of carboxylic acids groups.

Targeting of LPFFD-functionalized MNPs (MNP-PEG-LPFFD) to A $\beta$  aggregated for 12 hrs was confirmed via transmission electron microscopy (TEM) (Figure 3D). TEM images of A $\beta$  aggregates in the presence of MNPs coated with PEG alone (MNP-PEG) were used as controls (Figure 3C). Automated analysis of TEM images revealed specific binding of MNP-

PEG-LPFFD to A $\beta$  aggregates (27.4 $\pm$ 5.1 % area coverage), while little to no A $\beta$  coverage was observed for MNP-PEG (3.07 $\pm$ 0.59 % area coverage) (Figure 3E). The difference in A $\beta$  coverage by MNP-PEG-LPFFD versus MNP-PEG was found to be statistically significant with  $p=2.4\times 10^{-6}$ . The apparent non-uniformity of MNP-PEG-LPFFD binding to A $\beta$  is likely driven by magnetic interactions between the nanoparticles (**Figure 4**). DLS data (Figure 3B) indicates colloidal stability of MNPs in PBS, and hence we hypothesize that the observed MNP clustering takes place during binding to A $\beta$ , rather than in solution. As our MNPs exhibit significant magnetic moments and are coated in electrostatically neutral ligands, we anticipate that magnetic dipole interactions influence their collective behavior during binding. To investigate this effect, we developed a simple statistical model (Supporting Information) that considers the probability of a MNP binding to a specific site on the A $\beta$  backbone (Figure 4A) based on its interaction with other particles already bound to the same aggregate. Figure 4B illustrates a random distribution of MNPs on an A $\beta$  aggregate, neglecting magnetic interactions. To account for these interactions while adding particles to the grid stochastically, the random placement of each subsequent particle on an available site  $\{i,j\}$  can be weighted according to the probability  $p_{i,j}$ , which describes a random selection from a Boltzmann distribution of potential binding site energies:

$$p_{i,j} = \frac{\exp\left(-\frac{U_{i,j}}{k_B T}\right)}{Q} \quad (1)$$

where  $k_B$  is the Boltzmann constant,  $T$  is temperature, and  $Q$  is the partition function:

$$Q = \sum_{i,j}^{all\ available} \exp\left(-\frac{U_{i,j}}{k_B T}\right) \quad (2)$$

Here  $U_{i,j}$  represents the Zeeman energy of a hypothetical magnetic dipole  $\vec{m}_{i,j}$  added to an available site  $\{i,j\}$  and locally aligned with the net magnetic field from the other dipoles  $\vec{m}_1 \dots \vec{m}_p$  present on the grid:

$$U_{i,j} = \frac{-\mu_0 m}{4\pi} \left| \sum_n^p \left[ \frac{3(\vec{m}_n \cdot (\vec{r}_{i,j} - \vec{r}_n))(\vec{r}_{i,j} - \vec{r}_n)}{|\vec{r}_{i,j} - \vec{r}_n|^5} - \frac{\vec{m}_n}{|\vec{r}_{i,j} - \vec{r}_n|^3} \right] \right| \quad (3)$$

where  $\mu_0$  is the permeability of free space, and  $(\vec{r}_{i,j} - \vec{r}_n)$  represents the relative position vector between dipole  $\vec{m}_n$  and grid site  $\{i, j\}$ .

In assuming that the particles affixed to the grid are perfectly superparamagnetic, it is necessary to additionally consider how moments on the grid might influence the orientation of their neighbors. We studied two limiting cases: uncorrelated moments and fully correlated moments. Both incorporate magnetic interaction when adding particles, but in the former case, the orientation of the moments on the grid is randomized before each addition, whereas the latter case minimizes the energy of the ensemble before each particle is added. In contrast to the random distribution shown in Figure 4B, we find that when magnetic interactions are used to weight the pseudorandom addition of MNPs to the grid, the particles tend to form clusters (Figure 4C), especially when the moments of the ensemble are uncorrelated (Figure 4D). In the case of fully correlated moments, MNPs form smaller clusters and chains (Figure 4E, F) on the A $\beta$  backbone, as indicated by the reduced chain departure distance, the distance of a MNP from the line formed by the two previously added MNPs.

## 2.4. AMF-Induced Disaggregation of A $\beta$ Deposits

The efficacy of AMF-induced disaggregation of A $\beta$  deposits decorated with MNPs was corroborated by TEM image analysis of samples treated and not treated with AMF. Following a 12 hr aggregation period, A $\beta$  samples were decorated with MNP-PEG-LPFFD and either incubated for an additional 3 hrs or subjected to a 3 hr treatment with AMF. For untreated samples, TEM images show A $\beta$  aggregates decorated with MNPs and virtually no isolated MNPs or short fibrils (**Figure 5A**). In contrast, samples exposed to AMF display a significant diversity of fibril sizes, particularly short fibrils, small aggregates, and many MNPs-PEG-LPFFD detached from fibrils, suggesting fibril scission at points of local power dissipation (Figure 5B). Automated analysis of TEM images reveals an average aggregate size reduction



of 68% for samples treated with AMF (Figure 5C). In images of the control experiments, there is no significant change in aggregate size of A $\beta$  alone or A $\beta$  in the presence of PEG-MNPs with AMF exposure (Figure S4).

To avoid possible drying effects that may influence TEM image analysis, the hydrodynamic size distribution of 12-hr-old A $\beta$  aggregates was monitored for samples with and without 3 hr AMF exposure using DLS. We observed an order of magnitude decrease in average aggregate hydrodynamic radius for A $\beta$  targeted with MNP-PEG-LPFFD and AMF exposure compared to A $\beta$  alone, with a shift in peaks from 2008 nm and 367 nm (A $\beta$  alone) to 129 nm and 24 nm (A $\beta$  + MNP-PEG-LPFFD after AMF exposure) (Figure 5D). A significant change in hydrodynamic radius is not observed for control samples of A $\beta$  alone or A $\beta$  in the presence of PEG-MNPs after AMF exposure (Figure S5).

To further assess the potential of AMF and MNP mediated disruption of A $\beta$ , we allowed A $\beta$  to aggregate at physiological conditions for 168 hrs before exposure to AMF. Long incubation times led to the formation of large aggregates ( $> 5 \mu\text{m}$ ), which exceeded the detection limit of DLS, so TEM image analysis and ThT fluorescence assays were used to compare AMF-treated and non-treated 168 hr A $\beta$  samples decorated with MNP-PEG-LPFFD. In TEM images, for samples not treated with AMF, we observed large aggregates profusely decorated with MNPs (**Figure 6A**). Following 6 hr AMF exposure, we observed small fibrils, amorphous aggregates, and many MNPs detached from fibrils (Figure 6B). No significant difference upon AMF exposure was found in size and morphology for control samples that included A $\beta$  alone or A $\beta$  in the presence of MNP-PEG (Figure S6). A histogram generated from automated image analysis of A $\beta$  aggregate morphology reveals a clear shift to smaller aggregate sizes for AMF-treated samples, as all of the aggregate areas lie in the first bin, whereas the aggregates from the non-treated samples are distributed across larger area bins (Figure 6C). Reducing the bin size allows us to resolve the distribution of the aggregates following the AMF treatment, revealing the area range  $0.09 \times 10^5$ - $12 \times 10^5 \text{ nm}^2$  (Figure 6D).

The data presented in Figures 6C and 6D were not normally distributed as determined by a two-sample Kolmogorov-Smirnov test, and consequently Wilcoxon rank-sum test was performed to confirm statistical difference of the aggregate area distributions for AMF-treated and non-treated samples ( $p < 0.001$ ).<sup>[38]</sup>

The decrease in ThT fluorescence intensity for 168-hr-old A $\beta$  aggregates decorated with MNP-PEG-LPFFD following 6 hrs of AMF as compared to the samples incubated for 6 hrs at 37 °C without AMF exposure further confirms magnetothermal disruption of  $\beta$ -sheet structure (Figure 6E). The ThT fluorescence experiences a slight increase for pristine A $\beta$  samples, while A $\beta$  samples in the presence of untargeted MNP-PEG do not exhibit any notable change in ThT fluorescence. The former might be explained by the accelerated aggregation of A $\beta$  observed at elevated solution temperatures that may be reached during the AMF treatment.<sup>[39]</sup> (Fluctuations of  $\pm 2$  °C occur in our apparatus). The lack of ThT fluorescence intensity change in the A $\beta$  sample in the presence of untargeted MNP-PEG may stem from the competing aggregation at elevated temperatures and disaggregation induced by MNPs non-specifically trapped within some A $\beta$  aggregates. Similar trends in fluorescence were observed for 24-hr-old A $\beta$  exposed to 4 hrs of AMF (Figure S7).

## 2.5. Effect of Magnetothermal Disruption of A $\beta$ Aggregates on Neuronal Viability

While the biocompatibility of iron oxide MNPs has been established in numerous *in vitro* and *in vivo* studies,<sup>[29–32,34]</sup> including our earlier work,<sup>[40]</sup> here we aimed to evaluate the potential neurotoxic effects of magnetothermal disaggregation of A $\beta$ . Specifically, a number of reports indicate that soluble A $\beta$  oligomers may yield greater neurotoxicity than larger aggregates.<sup>[10,41–43]</sup> While our data presented in Figures 5 and 6 indicates that our method yields smaller A $\beta$  aggregates rather than oligomers, we have investigated the effects of magnetothermal A $\beta$  disaggregation on the viability of primary hippocampal neurons *in vitro*. To mimic the physiological environment, hippocampal neurons were incubated directly with

A $\beta$  aggregates (**Figure 7A**), and their viability was assessed in the presence of magnetothermal treatment (**Figure 7B**). We found that in the absence of MNPs, A $\beta$  aggregates led to a significant decrease in neuronal viability ( $\sim 70\%$  as compared to control cultures without A $\beta$ ) (**Figure 7B**). Interestingly, 3 hr application of AMF in the presence of MNPs targeted to A $\beta$  fibrils did not induce neurotoxic effects (neuronal viability  $\sim 95\%$ ). The untargeted MNPs also appear not to induce neurotoxic effects, which may be explained by the non-specific entrapment of MNP-PEG within the A $\beta$  aggregates. The colloidal stability of MNP-PEG may be reduced in the calcium ion and magnesium ion rich artificial cerebrospinal fluid as compared to PBS that was used for *in situ* experiments. Furthermore, due to magnetic interactions between MNPs, it is plausible that nonspecific entrapment would lead to clustering of MNPs on the fibrils enabling disaggregation in the presence of AMF.

## 2.6. Mechanisms of A $\beta$ Disaggregation

Solving a macroscopic heat transport equation for isolated MNP heat sources surrounded by water predicts a negligible temperature increase  $\ll 1$  °C – clearly insufficient to disrupt  $\beta$ -sheet structure.<sup>[44]</sup> This prediction, however, is contradicted by recent experimental evidence showing effective temperature increases on the order of 10s of °C within the first few nanometers of MNP surfaces,<sup>[45]</sup> making it plausible that MNPs decorating the A $\beta$  aggregates could generate significant local heating. Furthermore, based on the analysis of the TEM images (**Figure 3**) and the statistical model for the distribution of interacting magnetic dipoles (**Figure 4**), MNPs targeted to A $\beta$  deposits tend to form clusters. These MNP clusters can then produce more substantial collective heating of the surrounding protein matter than the individual MNPs.<sup>[46–48]</sup> Increased temperature is anticipated to excite vibrational modes within the A $\beta$  fibrils, leading to significant bending and tension that weakens hydrophobic interactions between fibrils and subsequently introduces defects into the aggregate.<sup>[49]</sup> This

hypothesis is supported by atomistic modeling suggesting that the strength properties of amyloid fibrils are highly length dependent, and fibrils approaching micrometer-length scale become increasingly mechanically weak, and tend to break even under minor thermal fluctuations.<sup>[2,49–51]</sup>

According to our image analysis, the MNP-mediated disaggregation of A $\beta$  aggregates does not produce soluble oligomers (3–10 nm in diameter), which are intermediates in the fibril formation pathway and have been hypothesized to confer synaptic dysfunction,<sup>[7–10,52–54]</sup> but it instead generates smaller fibrillar aggregates (~100–400 nm in diameter). Tuning the AMF and MNP parameters to produce aggregates of various sizes could be a useful platform for investigation of protein aggregation, and could potentially have therapeutic benefits, as the smaller aggregates generated by MNP cleavage are in the size range suitable for engulfment and clearance by microglia.<sup>[55,56]</sup>

### 3. Conclusion

We demonstrate a technique using remotely triggered local heating to disaggregate deposits of the small protein A $\beta$ <sub>(1–42)</sub>, which plays an important role in AD pathogenesis. Surface modification of ferrite MNPs enables specific targeting to protein aggregates, restricting the magnetothermal interrogation to the desired site under applied AMF. Biocompatibility assessment in primary hippocampal cultures indicates that exposure to MNPs and AMFs does not yield neurotoxic effects. Based on these findings, we suggest that the magnetothermal platform may serve as a safe and facile wireless tool for basic study of aggregation in protein misfolding systems.

### 4. Experimental Methods

*A $\beta$ <sub>(1–42)</sub> preparation:* A $\beta$ <sub>(1–42)</sub> was synthesized, purified, and characterized by Dr. James I. Elliott at Yale University (New Haven, CT). The peptide mass and purity were determined by

electrospray/ion trap mass spectrometry and purified by reverse phase high-performance liquid chromatography (HPLC), respectively. Aggregate free A $\beta$  monomer solution was prepared as described previously.<sup>[26]</sup> A $\beta$  peptide (1 mg) was dissolved at a concentration of 1 mg/ml in 50 mM Tris-HCl, pH 8.5 containing 7 M guanidinium-HCl and 5 mM EDTA, and incubated overnight at room temperature. The sample was centrifuged at 16,000 g for 30 minutes prior to injection onto a superdex 75 10/300 gel filtration column (GE Healthcare Biosciences, Piscatawa, NJ) connected to a DuoFlow FPLC (Bio-Rad, Hercules, CA). The peptide was eluted in 20 mM sodium phosphate, pH 8.0 at 0.5 mL/min while monitoring UV absorbance at 280 nm. Fractions (0.5 mL) were collected and A $\beta_{(1-42)}$  monomer containing fractions were pooled. The concentration of A $\beta$  in the pooled sample was determined by measuring the absorbance at 275 nm ( $\epsilon = 1361 \text{ M}^{-1} \text{ cm}^{-1}$ )<sup>[57]</sup> in a quartz cuvette (Starna Cells, Atascadero, CA) and using a SpectraMax M2 cuvette reader (Molecular Devices, Sunnyvale, CA). Peptide solution was diluted to 20  $\mu\text{M}$ , and 200  $\mu\text{L}$  aliquots were prepared in low protein binding tubes (Eppendorf, Hauppauge, NY). Aliquots were snap frozen on dry ice and stored at -80 °C.

*Nanoparticle Synthesis:* Monodisperse spherical  $22.0 \pm 0.7$  nm diameter Fe<sub>3</sub>O<sub>4</sub> MNPs were synthesized via thermal decomposition of metal-oleate precursors and made soluble in water via high-temperature phase transfer with poly(acrylic acid) as outlined previously in Chen et al.<sup>[28]</sup>

*AMF Experimental Setup:* The AMF experiments were performed on a custom AMF coil driven by a 200 W amplifier (Electronics & Innovation, Inc., 1020L). The coil consisted of a ferrite toroid (Ferroxcube, 3F3) machined to include a 0.75 cm gap and wrapped with 1050 strand 40-gauge litz wire (MWS Wire Industries) (Figure S8). An RLC resonance circuit (Figure S8) drove the circuit at 100 kHz, simultaneously exposing up to three 500  $\mu\text{L}$  sample tubes to the AMF. The field amplitude was measured by a custom-built inductive field probe employing a pickup loop and an oscilloscope (Agilent 33210A). Thermal effects of resistive

power dissipation by the wires and hysteretic core losses were offset by a simple cooling system circulating ice water to the coil via silicone tubing.

*AMF Test:* For all AMF experiments, A $\beta$ <sub>(1-42)</sub> was aggregated in PBS at 37°C for 12, 24, or 168 hrs, and immediately before performing the AMF test, functionalized MNPs were added to the solution. To test the effectiveness of the MNPs under AMF exposure, we prepared three types of samples, the first two of which act as controls: A $\beta$ , A $\beta$  + MNP-PEG, and A $\beta$  + MNP-PEG-LPFFD. Samples were prepared by mixing 108  $\mu$ L of 5  $\mu$ M A $\beta$  solution with 12  $\mu$ L of either H<sub>2</sub>O or 0.28 mg Fe/mL functionalized MNPs, which are diluted to a final concentration of 28  $\mu$ g Fe/mL MNP in the amyloid solution. Half of the volume (60  $\mu$ L) was then pipetted into each of the three low protein binding Eppendorf tubes that were placed into the gap of the toroid coil for the AMF experiment (Figure S8). The remaining 60  $\mu$ L of each sample was incubated at 37  $\pm$  2°C for the duration of the AMF test.

An AMF insensitive fiber optic temperature probe (Omega Engineering, Model: HHTFO-101) was secured to the Eppendorf tubes inside the gap to monitor the temperature throughout the AMF experiment and ensure it was maintained at 37  $\pm$  2°C.

*Conjugation Chemistry:* LPFFD peptide was synthesized using Intavis Model MultiPep multiple peptide synthesizer and purified using HPLC. The MNPs stabilized with PAA were suspended in 10<sup>-2</sup> M EDC and 10<sup>-2</sup> M NHS solution at pH 5.6 for 30 min to activate carboxylic groups. For PEG (10 kDa) immobilization, MNPs were precipitated by centrifugation at 13,000 rpm for 10 min and resuspended in a solution of 5 mg/mL of heterobifunctional PEG (NH<sub>2</sub>-PEG-COOH) (Laysan Bio Inc.) in a 10<sup>-2</sup> M EDC and 10<sup>-2</sup> M NHS solution at pH 8.6 under mechanical stirring for 24 h. For LPFFD grafting, PEG-MNPs (1 mg/mL) were incubated in a solution of 1 mg/mL of LPFFD in a 10<sup>-2</sup> M EDC and 10<sup>-2</sup> M NHS solution at pH 8.6 under mechanical stirring. After 24 h, the MNPs were rinsed 5 times with PBS.

*Statistical model:* The statistical model of MNP distribution on the A $\beta$  substrates (Figure 4) was carried out using Wolfram Mathematica 10 software,<sup>[58]</sup> and ImageJ<sup>[59]</sup> was used to threshold TEM images. Details of the simulation design are in the Supporting Text.

*Thioflavin T (ThT) Fluorescence Assay:* 2 mM ThT (Sigma) was prepared in purified water, filtered through a 0.22  $\mu$ m filter and aliquots prepared and frozen at -20°C as a 100x stock. To prepare samples for fluorescence measurements, a 1:100 dilution of ThT stock was made into the amyloid sample. Amyloid samples were incubated under physiological conditions to a desired aggregation state. Immediately before fluorescence measurement, 0.5  $\mu$ L ThT was added to the sample and each 50  $\mu$ L sample was pipetted into multiple wells of a 96-well half-area plate of black polystyrene with black bottom and nonbinding surface (Corning 3993). ThT fluorescence was measured from the top of the plate in a microplate reader (Tecan Infinite Pro M200). Because ThT fluorescence intensity shifts from yellow to red when it binds A $\beta$ , we subtracted the fluorescence intensity of ThT in PBS from the fluorescence intensities of amyloid samples in order to eliminate any possible fluorescence overlapping effect from ThT in solution.

*Dynamic Light Scattering (DLS):* MNPs were removed from samples via magnetic separation, and the supernatants were transferred to disposable polystyrene micro cuvettes (ZEN0118 from Malvern) on ice and immediately analyzed by DLS. Measurements were made using a Nano ZetaSizer (MALVERN Nano-ZS90, UK) comprising a 50 mW 633 nm laser. Light scattering was measured at 90°. The intensity correlation function and the distribution of the R<sub>H</sub> (hydrodynamic radii) of the particles contributing to the scattering were determined using MALVERN ZetaSizer Software. All of our DLS measurements received the “Result Meets Quality Criteria” report, and therefore we received a “Good” Size Quality Report for each measurement overall.

*TEM Sample Preparation:* Negative-staining TEM was used to visualize A $\beta$ . 10  $\mu$ L of each sample was adsorbed for 10 min onto carbon-coated copper grids (Ted Pella, Inc.) and gently

wicked away with filter paper. 10  $\mu$ L of freshly filtered 2% uranyl acetate staining solution was then adsorbed for 2 min onto the grid and gently wicked off. Grids were allowed to dry in a light-protected environment for several minutes before being imaged on a Tecnai G2 Spirit TWIN electron microscope at 120 kV.

*Image Analysis/Thresholding:* To evaluate targeting capability of MNPs, we used ImageJ<sup>[59]</sup> software to set a threshold for TEM image analysis, which we used to extract the MNP coverage of the aggregates. To calculate the area of the fibrils from the TEM images, we set the upper threshold by finding the mean pixel value of the background of the image and subtracting three standard deviations from this mean ( $3\sigma$ ). An identical process involving the mean pixel value and  $3\sigma$  of the fibrils was used to calculate the area of the MNPs (Figure S9). To analyze size distribution of aggregates for samples treated with AMF, the “Analyze Particles...” command in ImageJ 1.47c under the Analyze tab on the toolbar was used to bin the areas of aggregates in TEM images from each test group. Further analysis was performed in MATLAB (The MathWorks Inc.) with routines from the Statistics Toolbox.

*In vitro AMF treatment:* For the *in vitro* AMF experiments, primary hippocampal neurons were seeded onto 5mm round-coverslips coated with matrigel at a density of 10,000 cells per coverslip.  $A\beta_{(1-42)}$  was aggregated in PBS at 37°C for 12 hrs.  $A\beta$  aggregates were prepared as described previously for disaggregation in solution. The aggregated  $A\beta$  solution ( $A\beta$ ,  $A\beta$  + MNP-PEG, or  $A\beta$  + MNP-PEG-LPFFD) was dropped into the hippocampal neuron’s culture at a final concentration of 5  $\mu$ M in Tyrode. Hippocampal neurons incubated with the different  $A\beta$  solutions were treated for 3h with AMF at the field conditions previously described (Figure S10A). An AMF insensitive fiber optic temperature probe was secured inside the cell sample holder to monitor the temperature throughout the AMF experiment to ensure it was maintained at  $34 \pm 1^\circ\text{C}$  (Figure S10B).

*Confocal Imaging:* Primary hippocampal neurons were seeded onto 5 mm round-coverslips coated with matrigel at a density of 10,000 cells per coverslip. Viral transfection was achieved



by adding 1  $\mu$ L (109 transducing units/mL) of *Lenti-CamKII $\alpha$ ::mCherry* followed by a 5 day induction period. A $\beta$  was stained with thioflavin T (ThT) following the procedure previously described. The aggregated A $\beta$  stained with ThT was dropped into the cell culture and imaged in Tyrode's solution using a water immersion 40X objective.

*Cell Viability Assay:* Cell viability was determined by the colorimetric MTT assay. Primary hippocampal neurons were cultured as described before for CLSM imaging. After 3h AMF treatment, each coverslip was placed into each well of 96-well plates with 200  $\mu$ L of neurobasal culture media. Thiazolyl Blue Tetrazolium Bromide (TT) was dissolved in Tyrode's solution at a concentration of 5 mg/mL. Then, 20  $\mu$ L of TT solution was added into each well and incubated for 3 hours. Then the supernatant was aspirated and 200  $\mu$ L of dimethyl sulfoxide (DMSO) was added. The absorbance was measured by means of a plate reader at 550 nm. *Statistics:* Each condition was measured using 6 sample replicates and statistical significance was tested by ANOVA and Tukey test.

### Supporting Information

Supporting Information is available from the Wiley Online Library or from the author.

### Acknowledgements

Authors thank Y. Wang and A. Lomakin for their advice on dynamic light scattering, M. Buehler for his insight into mechanisms of amyloid disaggregation, the Koch Institute Biopolymers and Proteomics core facility for synthesizing the targeting peptide sequence (LPFFD), and the Biophysical Instrumentation Facility for the Study of Complex Macromolecular Systems (NSF-007031).

This work was supported in part by the MIT MRSEC through the MRSEC Program of the National Science Foundation (NSF) under award number DMR-0819762, the NSF CAREER Award (CBET-1253890), and the Defense Advanced Research Projects Agency (DARPA) Young Faculty Award (D13AP00045).

The manuscript was written through contributions of all authors. All authors have given approval to the final version of the manuscript.

Received: ((will be filled in by the editorial staff))

Revised: ((will be filled in by the editorial staff))

Published online: ((will be filled in by the editorial staff))

## References

- [1] F. Chiti, C. M. Dobson, *Annu. Rev. Biochem.* **2006**, 75, 333.
- [2] T. Knowles, M. Buehler, *Nat. Nanotechnol.* **2011**, 1.
- [3] R. Paparcone, M. J. Buehler, *Appl. Phys. Lett.* **2009**, 94, 243904.
- [4] J. Hardy, D. J. Selkoe, *Science* **2002**, 297, 353.
- [5] E. Karran, M. Mercken, B. De Strooper, *Nat. Rev. Drug Discov.* **2011**, 10, 698.
- [6] G. Leinenga, J. Götz, *Sci. Transl. Med.* **2015**, 7.
- [7] C. Haass, D. J. Selkoe, *Nat. Rev. Mol. Cell Biol.* **2007**, 8, 101.
- [8] J. P. Cleary, D. M. Walsh, J. J. Hofmeister, G. M. Shankar, M. a Kuskowski, D. J. Selkoe, K. H. Ashe, *Nat. Neurosci.* **2005**, 8, 79.
- [9] C. G. Glabe, *J. Biol. Chem.* **2008**, 283, 29639.
- [10] M. P. Lambert, a K. Barlow, B. a Chromy, C. Edwards, R. Freed, M. Liosatos, T. E. Morgan, I. Rozovsky, B. Trommer, K. L. Viola, P. Wals, C. Zhang, C. E. Finch, G. a Krafft, W. L. Klein, *Proc. Natl. Acad. Sci. U. S. A.* **1998**, 95, 6448.
- [11] C. Soto, E. M. Sigurdsson, L. Morelli, R. A. Kumar, E. M. Castaño, B. Frangione, *Nat. Med.* **1998**, 4, 822.
- [12] Q. Nie, X. Du, M. Geng, *Acta Pharmacol. Sin.* **2011**, 32, 545.
- [13] A. Bellova, E. Bystrenova, M. Koneracka, P. Kopcansky, F. Valle, N. Tomasovicova, M. Timko, J. Bagelova, F. Biscarini, Z. Gazova, *Nanotechnology* **2010**, 21, 065103.
- [14] M. Mahmoudi, F. Quinlan-Pluck, M. P. Monopoli, S. Sheibani, H. Vali, K. a Dawson, I. Lynch, *ACS Chem. Neurosci.* **2013**, 4, 475.
- [15] M. J. Kogan, N. G. Bastus, R. Amigo, D. Grillo-Bosch, E. Araya, A. Turiel, A. Labarta, E. Giralt, V. F. Puentes, *Nano Lett.* **2006**, 6, 110.
- [16] E. Araya, I. Olmedo, N. G. Bastus, S. Guerrero, V. F. Puentes, E. Giralt, M. J. Kogan, *Nanoscale Res. Lett.* **2008**, 3, 435.
- [17] N. G. Bastus, M. J. Kogan, R. Amigo, D. Grillo-Bosch, E. Araya, A. Turiel, A. Labarta, E. Giralt, V. F. Puentes, *Mater. Sci. Eng. C* **2007**, 27, 1236.
- [18] M. Li, X. Yang, J. Ren, K. Qu, X. Qu, *Adv. Mater.* **2012**, 24, 1722.

- [19] C. Adura, S. Guerrero, E. Salas, L. Medel, A. Riveros, J. Mena, J. Arbiol, F. Albericio, E. Giralt, M. J. Kogan, *ACS Appl. Mater. Interfaces* **2013**, 5, 4076.
- [20] C. E. Tedford, S. DeLapp, S. Jacques, J. Anders, *Lasers Surg. Med.* **2015**, 47, 312.
- [21] R. Weissleder, *Nat. Biotechnol.* **2001**, 19.
- [22] K. Maier-Hauff, F. Ulrich, D. Nestler, H. Niehoff, P. Wust, B. Thiesen, H. Orawa, V. Budach, A. Jordan, *J. Neurooncol.* **2011**, 103, 317.
- [23] R. Khurana, C. Coleman, C. Ionescu-Zanetti, S. a Carter, V. Krishna, R. K. Grover, R. Roy, S. Singh, *J. Struct. Biol.* **2005**, 151, 229.
- [24] H. Levine, *Protein Sci.* **1993**, 404.
- [25] M. Bourhim, M. Kruzel, T. Srikrishnan, T. Nicotera, *J. Neurosci. Methods* **2007**, 160, 264.
- [26] E. Hellstrand, B. Boland, D. M. Walsh, S. Linse, *ACS Chem. Neurosci.* **2010**, 1, 13.
- [27] A. Lomakin, D. B. Teplow, *Methods Mol. Biol.* **2012**, 849, 69.
- [28] R. Chen, M. G. Christiansen, P. Anikeeva, *ACS Nano* **2013**, 7, 8990.
- [29] S. Laurent, D. Forge, M. Port, A. Roch, C. Robic, L. Vander Elst, R. N. Muller, *Chem. Rev.* **2008**, 2064.
- [30] A. Cole, A. David, J. Wang, C. Galban, V. Yang, *Biomaterials* **2011**, 32, 6291.
- [31] L. L. Muldoon, M. Sandor, K. E. Pinkston, E. A. Neuwelt, *Neurosurgery* **2005**, 57.
- [32] J. S. Weinstein, C. G. Varallyay, E. Dosa, S. Gahramanov, B. Hamilton, W. D. Rooney, L. L. Muldoon, E. A. Neuwelt, *J. Cereb. Blood Flow Metab.* **2010**, 30, 15.
- [33] R. Hergt, S. Dutz, *J. Magn. Magn. Mater.* **2007**, 311, 187.
- [34] K. Hervé, L. Douziech-Eyrolles, E. Munnier, S. Cohen-Jonathan, M. Soucé, H. Marchais, P. Limelette, F. Warmont, M. L. Saboungi, P. Dubois, I. Chourpa, *Nanotechnology* **2008**, 19, 465608.
- [35] C. Adessi, M.-J. Frossard, C. Boissard, S. Fraga, S. Bieler, T. Ruckle, F. Vilbois, S. M. Robinson, M. Mutter, W. a Banks, C. Soto, *J. Biol. Chem.* **2003**, 278, 13905.
- [36] A. T. Petkova, Y. Ishii, J. J. Balbach, O. N. Antzutkin, R. D. Leapman, F. Delaglio, R. Tycko, *Proc. Natl. Acad. Sci. U. S. A.* **2002**, 99, 16742.
- [37] R. Tycko, *Curr. Opin. Struct. Biol.* **2004**, 14, 96.
- [38] G. Van Belle, L. D. Fisher, *Biostatistics: A Methodology for the Health Sciences*, **2004**.

- [39] M. Ghavami, M. Rezaei, R. Ejtehad, M. Lotfi, M. a Shokrgozar, B. Abd Emamy, J. Raush, M. Mahmoudi, *ACS Chem. Neurosci.* **2013**, *4*, 375.
- [40] R. Chen, G. Romero, M. G. Christiansen, A. Mohr, P. Anikeeva, *Science (80-. )*. **2015**, *347*, 1477.
- [41] D. M. Walsh, D. J. Selkoe, *J. Neurochem.* **2007**, *101*, 1172.
- [42] D. M. Walsh, I. Klyubin, J. V Fadeeva, M. J. Rowan, D. J. Selkoe, *Biochem. Soc. Trans.* **2002**, *30*, 552.
- [43] I. Benilova, E. Karran, B. De Strooper, *Nat. Neurosci.* **2012**, *15*, 349.
- [44] P. Keblinski, D. G. Cahill, A. Bodapati, C. R. Sullivan, T. A. Taton, *J. Appl. Phys.* **2006**, *100*.
- [45] A. Riedinger, P. Guardia, A. Curcio, M. A. Garcia, R. Cingolani, L. Manna, T. Pellegrino, *Nano Lett.* **2013**, *13*, 2399.
- [46] C. L. Dennis, a. J. Jackson, J. a. Borchers, R. Ivkov, a. R. Foreman, J. W. Lau, E. Goernitz, C. Gruettner, *J. Appl. Phys.* **2008**, *103*, 7.
- [47] L. C. Branquinho, M. S. Carrião, A. S. Costa, N. Zufelato, M. H. Sousa, R. Miotto, R. Ivkov, A. F. Bakuzis, *Sci. Rep.* **2013**, *3*, 2887.
- [48] D. Serantes, K. Simeonidis, M. Angelakeris, O. Chubykalo-Fesenko, M. Marciello, M. Del Puerto Morales, D. Baldomir, C. Martinez-Boubeta, *J. Phys. Chem. C* **2014**, *118*, 5927.
- [49] Z. Xu, R. Paparcone, M. J. Buehler, *Biophysj* **2010**, *98*, 2053.
- [50] M. Solar, M. J. Buehler, *J. Mech. Behav. Biomed. Mater.* **2013**, *19*, 43.
- [51] R. Paparcone, M. J. Buehler, *Biomaterials* **2011**, *32*, 3367.
- [52] P. Cizas, R. Budvytyte, R. Morkuniene, R. Moldovan, M. Lösche, G. Niaura, G. Valincius, *Arch Biochem Biophys* **2011**, *496*, 84.
- [53] M. Ahmed, J. Davis, D. Aucoin, T. Sato, S. Ahuja, S. Aimoto, J. I. Elliott, W. E. Van Nostrand, S. O. Smith, *Nat. Struct. Mol. Biol.* **2010**, *17*, 561.
- [54] J. C. Stroud, C. Liu, P. K. Teng, D. Eisenberg, *Proc. Natl. Acad. Sci. U. S. A.* **2012**, *109*, 7717.
- [55] D. M. Paresce, R. N. Ghosh, F. R. Maxfield, *Neuron* **1996**, *17*, 553.
- [56] D. Schenk, *Nat. Rev. Neurosci.* **2002**, *3*, 821.
- [57] T. T. O'Malley, N. A. Oktaviani, D. Zhang, A. Lomakin, B. O'Nuallain, S. Linse, G. B. Benedek, M. J. Rowan, F. a a Mulder, D. M. Walsh, *Biochem. J.* **2014**, *461*, 413.

- [58] Wolfram Research, **2015**.
- [59] C. a Schneider, W. S. Rasband, K. W. Eliceiri, *Nat. Methods* **2012**, 9, 671.
- [60] M. G. Christiansen, A. W. Senko, R. Chen, G. Romero, P. Anikeeva, *Appl. Phys. Lett.* **2014**, 104.
- [61] N. Sreerama, S. Y. Venyaminov, R. W. Woody, *Protein Sci.* **1999**, 8, 370.
- [62] K. L. Linegar, a. E. Adeniran, a. F. Kostko, M. a. Anisimov, *Colloid J.* **2010**, 72, 279.

## Figures

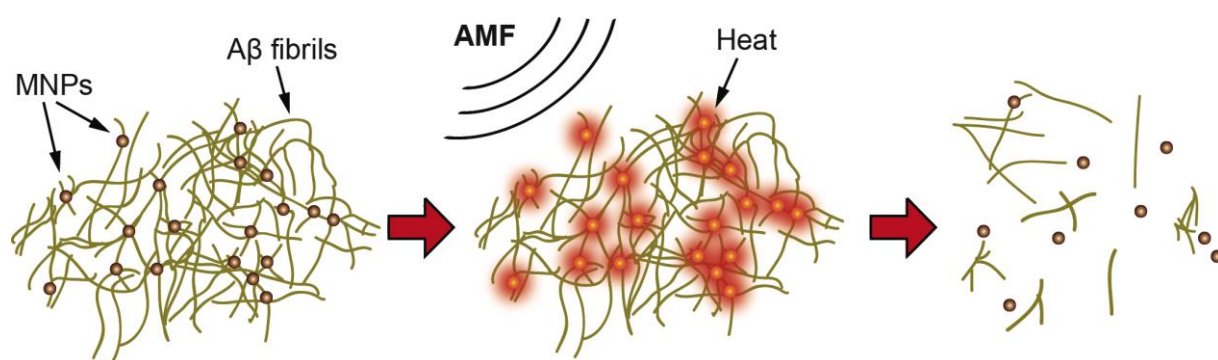


**Figure 1.** Method for remote protein disaggregation using alternating magnetic field (AMF) and magnetic nanoparticles (MNPs). In the presence of AMF, targeted MNPs dissipate heat that leads to fragmentation of amyloid aggregates.

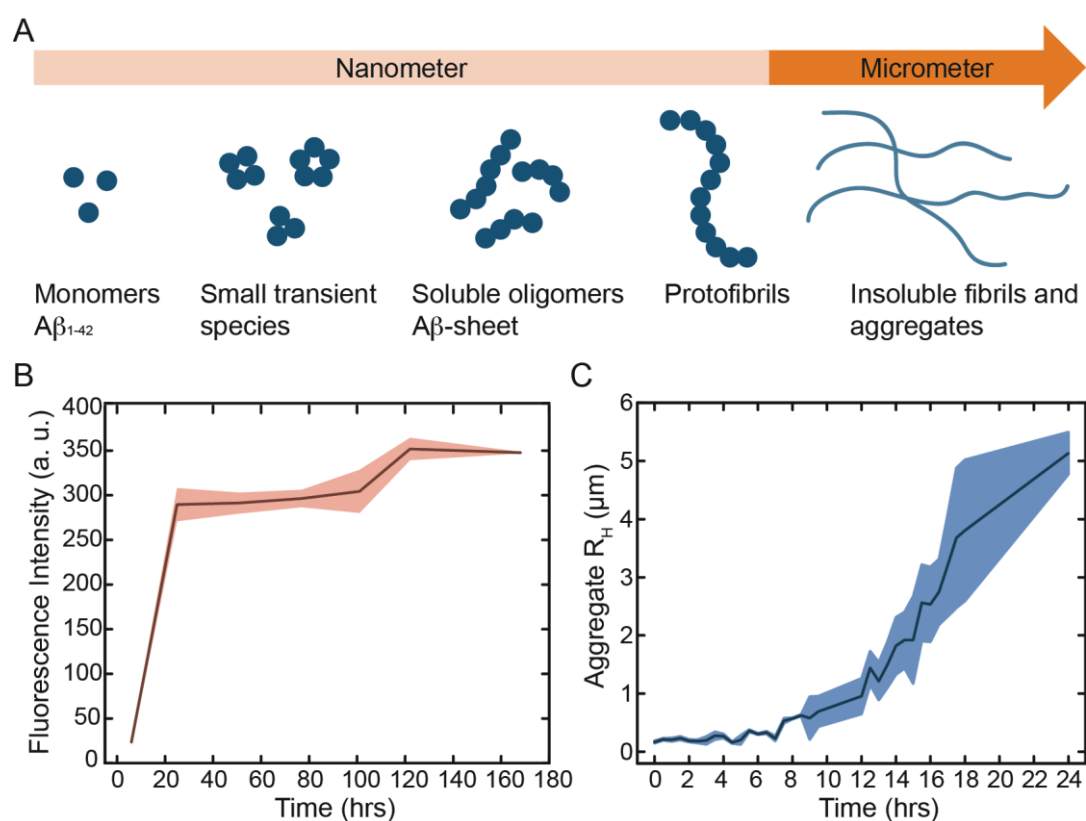


**Figure 2.** (A)  $A\beta$  monomers undergo a nucleation and growth process to form fibrils with a  $\beta$ -sheet structure that self-assembles into insoluble micrometer-scale aggregates. (B) ThT fluorescence follows  $A\beta_{(1-42)}$  aggregation kinetics ( $n=4$  trials at concentration  $5 \mu M$ , gain is

150 for all time points and trials). (C) DLS is used to measure average aggregate size over 24 hrs.

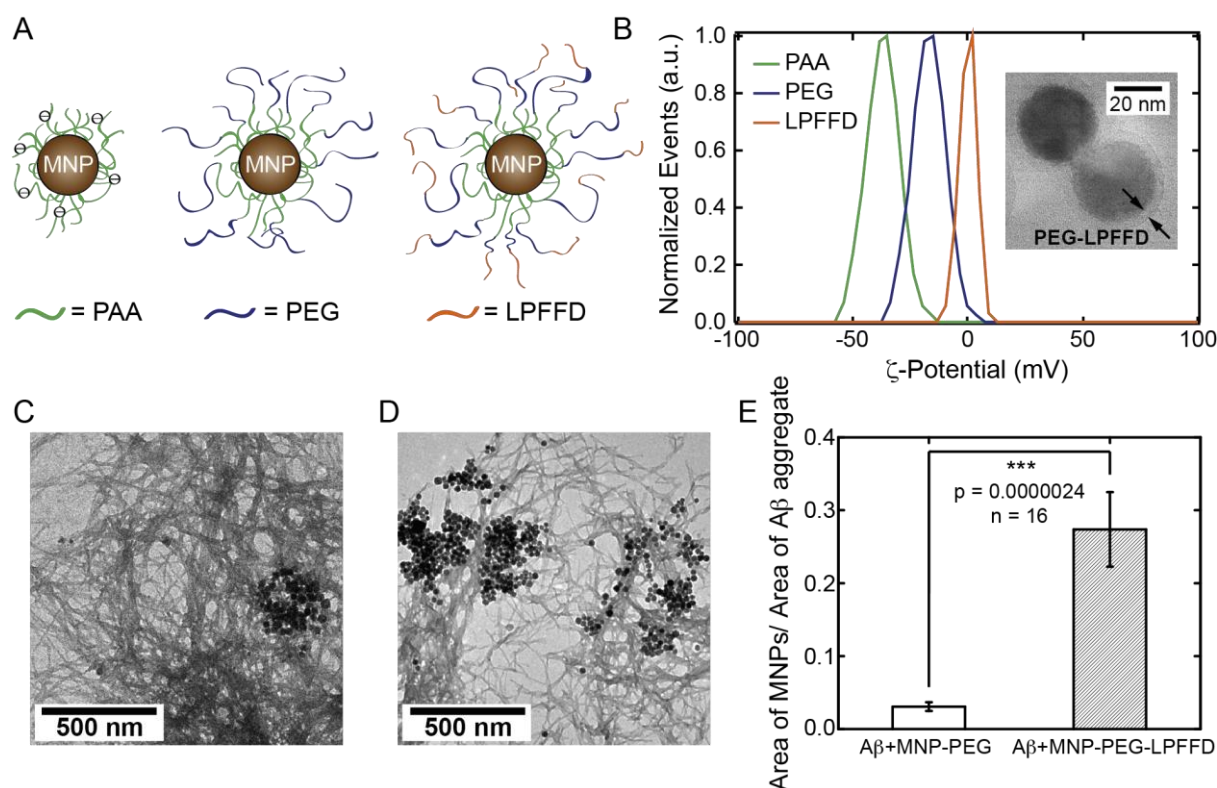


**Figure 3.** Functionalization of MNPs for stabilization in physiological conditions (PEG) and selective binding to A $\beta$  (LPFFD). (A) Carbodiimide chemistry is used to graft bi-functional PEG and LPFFD targeting sequence to Fe<sub>3</sub>O<sub>4</sub> MNPs. (B) Conjugation of ligands to MNPs is confirmed by a shift to neutral values of zeta potential. Inset: TEM image of functionalized MNPs with ~ 5 nm organic corona. (C), (D) TEM images of A $\beta$  with PEG-coated MNPs (C) and MNPs functionalized with LPFFD (D). (E) Fraction of MNP coverage of A $\beta$  aggregates. Image analysis reveals  $27.4 \pm 5.1$  % targeted MNP-PEG-LPFFD area coverage of A $\beta$  compared to  $3.07 \pm 0.59$  % area coverage for untargeted MNP-PEG. Number of analyzed TEM images  $n = 16$ , Student's t-test  $p = 2.4 \times 10^{-6}$ .

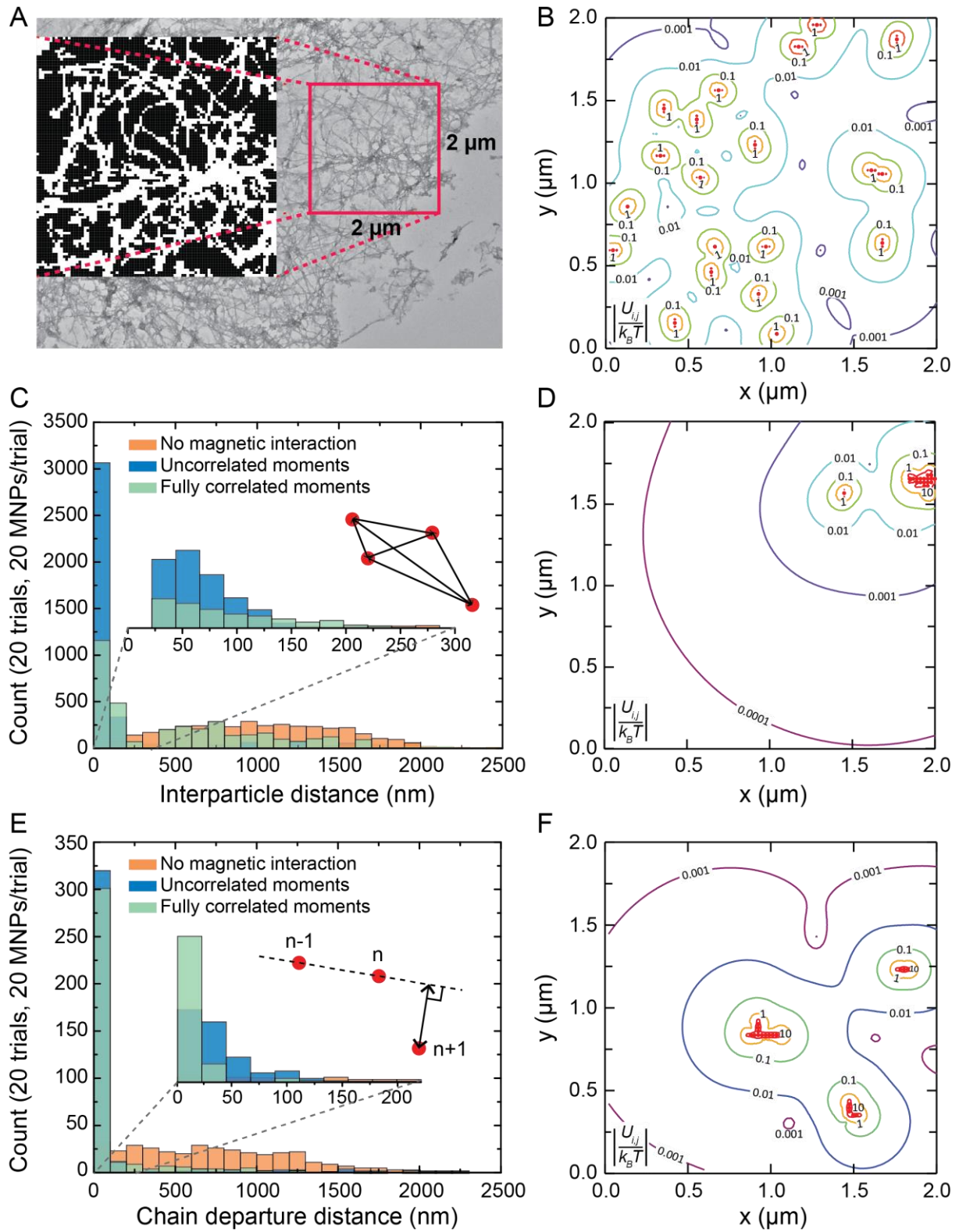


**Figure 4.** (A) A TEM image and the corresponding grid (inset), produced by setting thresholds for A $\beta$  fibrils. The grid step is 22 nm, corresponding to MNP physical diameter. White pixels denote available binding sites, whereas the black pixels indicate unavailable



sites, i.e. solution. (B) An example of the distribution of MNPs on the grid in (A) resulting from random placement without magnetic interaction. A contour plot of the energy of a test dipole locally aligned with the field and normalized to the thermal energy is shown. (C) The histogram illustrates the distribution of interparticle distances (inset graphic: black lines connecting the MNPs shown with red circles) for MNPs placed onto A $\beta$  grid in the absence of magnetic interaction (orange) and in the presence of magnetic interaction for uncorrelated (blue) and fully correlated (green) ensembles of MNPs. This histogram illustrates that the presence of magnetic interaction favors formation of MNP clusters, especially when the moments of the MNP ensemble are uncorrelated. Inset: The histogram with 22 nm bins resolves the distribution of distances < 300 nm. (D) An example contour plot similar to one in (B) illustrates clustering of MNPs on A $\beta$  grid in the presence of magnetic interaction with uncorrelated moments. (E) This histogram illustrates the distribution of chain-departure distances (inset graphic: black arrow orthogonally connecting an MNP to a dashed line between MNPs forming a chain) for the MNPs placed onto the A $\beta$  grid in the absence of magnetic interaction (orange) and in the presence of magnetic interaction without (blue) and with (green) correlation between the MNP magnetic moments. Taking a local correlation between moments in the MNP ensemble into account yields a strong preference for the formation of chains. Inset: The histogram with 22 nm bins resolves the distribution of distances < 220 nm. (F) An example contour plot similar to ones in (B) and (D) illustrates chain formation of MNPs on A $\beta$  grid in the presence of magnetic interaction with moments fully correlated with the local magnetic field.

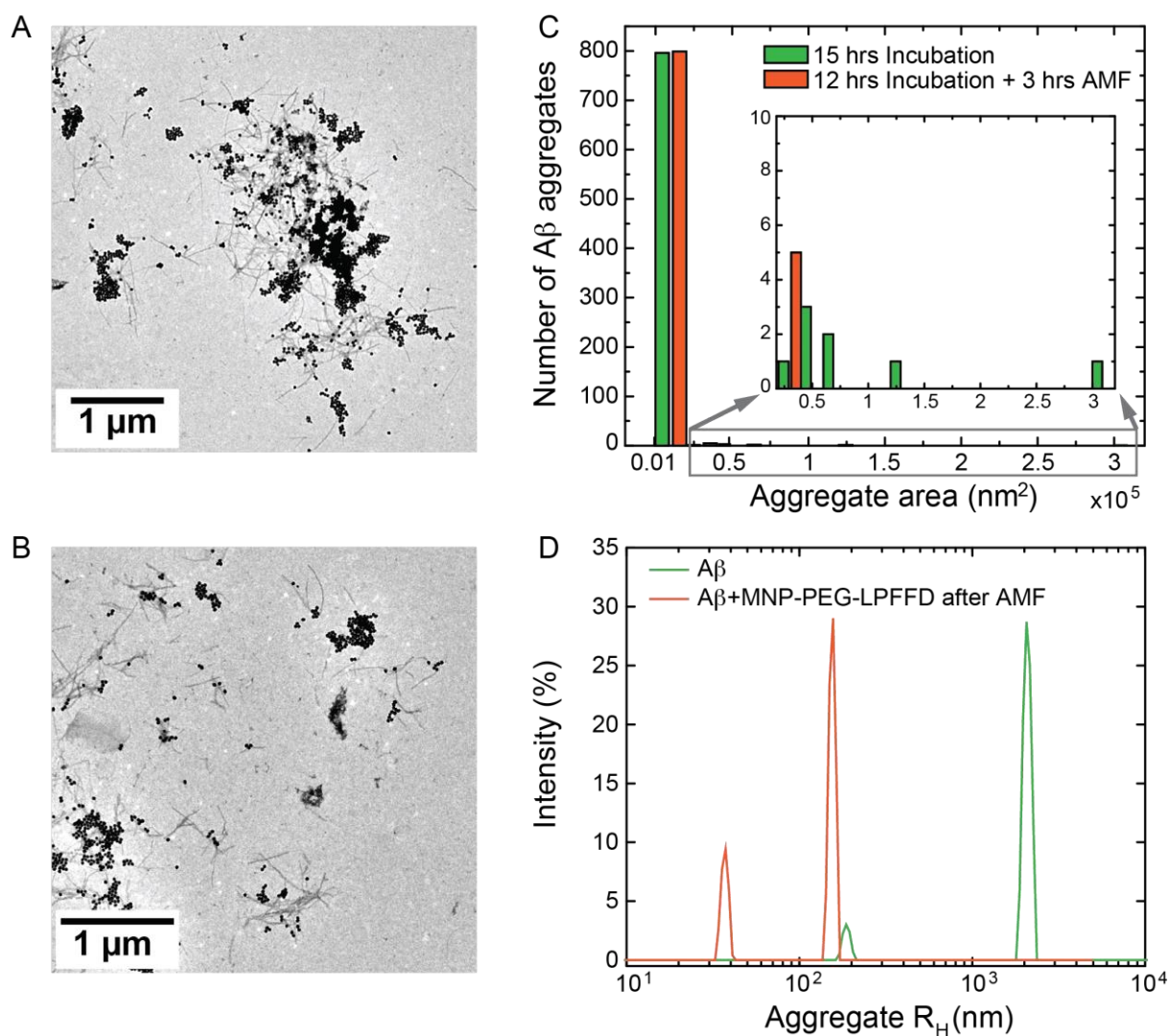


**Figure 5.** (A), (B) Representative TEM images of Aβ (12 hrs) decorated with MNP-PEG-LPFFD treated with (A) an additional 3 hrs of incubation at 37°C or (B) exposure to 3 hrs of AMF. (C) Histogram of the areas of aggregates analyzed from 8 randomly selected TEM images from each sample set. AMF-exposed samples (orange) and no AMF exposure (green). (D) DLS is used to measure the average aggregate size for Aβ alone with no AMF exposure (green), mean value:  $1191 \pm 198$  nm and Aβ + MNP-PEG-LPFFD after exposure (orange) to 3 hr AMF, mean value:  $387 \pm 12.5$  nm.

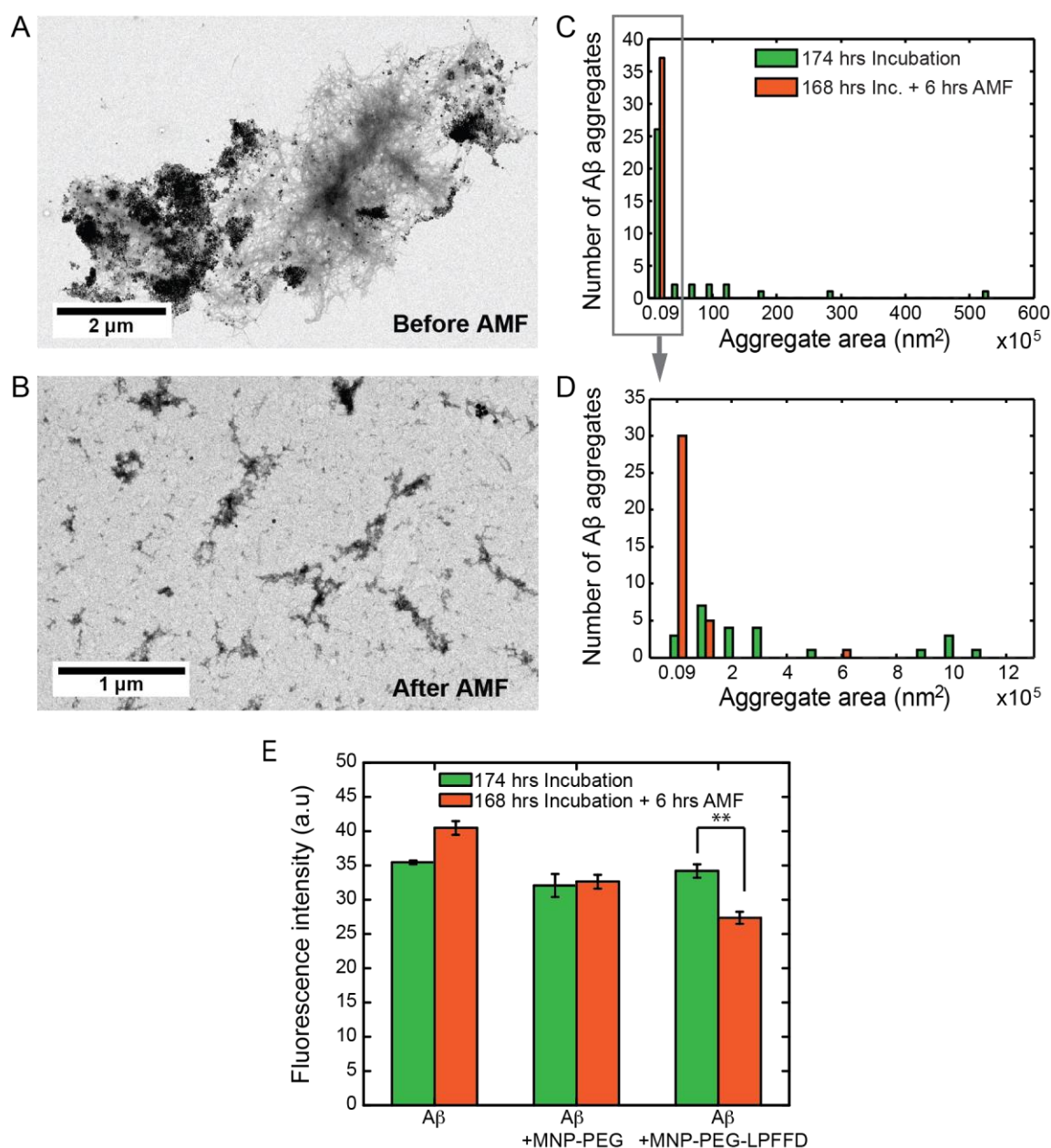


**Figure 6.** (A), (B) Representative TEM images of Aβ (168 hrs) decorated with MNP-PEG-LPFFD, (A) untreated and (B) treated with 6 hrs of AMF. (C) Histogram of the areas of 37 randomly selected aggregates (n = 8 images) from AMF-treated (orange) and untreated samples (green). (D) Areas binned into smaller intervals to examine distribution of AMF-treated samples. (E) Fluorescence intensity of AMF-treated (orange) and untreated (green) samples (Gain = 177). A decrease in intensity is observed for Aβ targeted with MNP-PEG-LPFFD following AMF, correlated with the disruption of the β-sheet structure. Number of trials n = 3, Student's t-test p = 0.003.

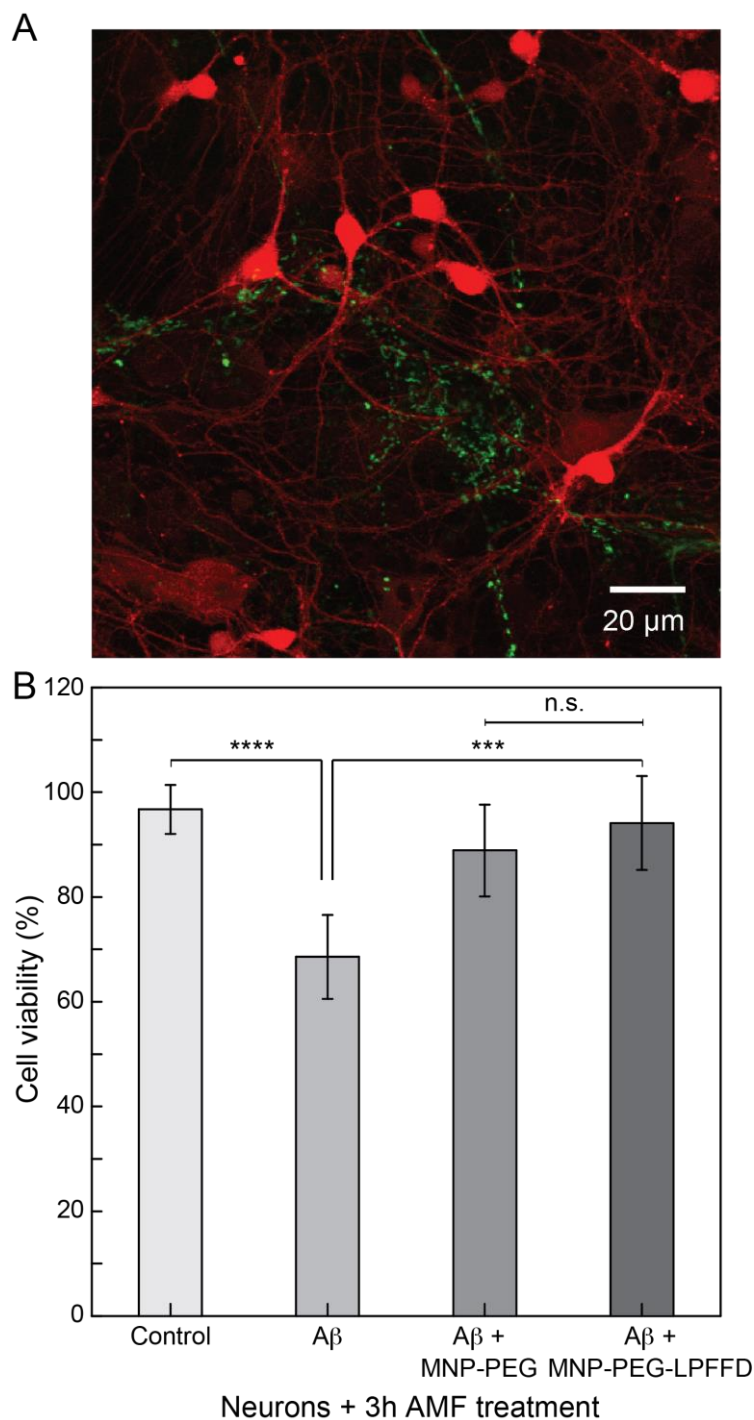


**Figure 7.** (A) Confocal image of hippocampal neurons incubated with A $\beta$  aggregates. Neurons were transfected with mCherry (red) and A $\beta$  was stained with thioflavin T (green). (B) Cell viability assessed by MTT assay of hippocampal neurons after 3h AMF treatment (control), and after 3h AMF treatment in presence of A $\beta$ , A $\beta$ +MNPs-PEG or A $\beta$ +MNPs-PEG-LPFFD.

## Supporting Information

**Title** Targeted Magnetic Nanoparticles for Remote Magnetothermal Disruption of Amyloid- $\beta$  Aggregates

*Colleen N. Loynachan,<sup>1</sup> Gabriela Romero,<sup>2</sup> Michael G. Christiansen,<sup>1</sup> Ritchie Chen,<sup>1</sup> Rachel Ellison,<sup>1</sup> Tiernan T. O'Malley,<sup>3</sup> Ulrich P. Froriep,<sup>2</sup> Dominic M. Walsh,<sup>3</sup> and Polina Anikeeva<sup>1,2\*</sup>*

### Supporting Text

TEMs such as the examples shown in Figures 3D and S3 indicate that the magnetic nanoparticles in this study tend to occur in clusters when bound to A $\beta$  aggregates. This raises the question of whether these clusters form before binding to the A $\beta$ , casting doubt on their stability in solution, or whether the clusters form during the process of binding to the A $\beta$ . While DLS data shown in Figure 3B contradicts the hypothesis that the magnetic nanoparticles in this study spontaneously form large clusters in solution, this information alone does not explain how stably suspended, superparamagnetic nanoparticles can cluster upon binding. To offer a possible explanation, we have employed a simple conceptual model that makes use of physical data directly relevant to the experiments described in the main text.

The model begins with a two dimensional grid of available sites, arranged in a pattern originating from a thresholded TEM of undecorated A $\beta$  fibrils, as shown in Figure 4A. For simplicity and to prevent overlap, the grid spacing was taken to be the physical diameter  $d_{phys}$  of the nanoparticles, 22.0nm ( $\pm 0.7$ ), as previously measured by TEM. A magnetic nanoparticle added to this grid can be described by its position and the orientation of its moment. The Zeeman energy of a trial dipole  $\vec{m}_t$  in the field of a source dipole  $\vec{m}_s$  can be written generally as follows:

$$U_{Zeeman} = \frac{-\mu_0}{4\pi} \left\{ \vec{m}_t \cdot \left[ \frac{3(\vec{m}_s \cdot \vec{r})\vec{r}}{|\vec{r}|^5} - \frac{\vec{m}_s}{|\vec{r}|^3} \right] \right\} \quad (1)$$

Where  $\mu_0$  is the permeability of free space (which is essentially unchanged in water) and  $\vec{r}$  is the position of the trial dipole relative to  $\vec{m}_s$ . Relative position  $\vec{r}$  is expressible in terms of the grid positions of the trial dipole  $\vec{r}_t$  and source dipole  $\vec{r}_s$ :

$$\vec{r} = \vec{r}_t - \vec{r}_s \quad (2)$$

If the moments of the source and trial dipoles are both equal to  $|\vec{m}|$  and the trial dipole is assumed to be locally aligned with the source dipole's field, its minimal energy configuration, then equation 1 reduces to:

$$U_{Zeeman} = \frac{-\mu_0 m^2}{4\pi} \left[ \frac{3(\hat{m}_s \cdot \hat{r}) - 1}{|\vec{r}|^3} \right] \quad (3)$$

A population averaged magnetic moment can be inferred by measuring susceptibility of a nanoparticle sample in solution in the low field limit with a vibrating sample magnetometer. To put this quantity in intuitive terms, we employ the concept of “magnetic diameter”  $d_m$ , or the diameter corresponding to an idealized, uniformly magnetized sphere with bulk saturation magnetization  $M_s$  and an identical moment  $m$ .<sup>[60]</sup>

$$d_m = \sqrt[3]{\frac{6m}{\pi M_s}} \quad (4)$$

The magnetic diameter of the particles used for all data shown in the main text was found to be smaller than the physical diameter, or approximately 18.8nm, assuming a saturation magnetization of magnetite,  $4.7 \times 10^5 \text{ Am}^{-1}$ .

Dividing  $U_{Zeeman}$  by the ambient thermal energy and converting the units of distance on the grid into meters suggests a convenient unitless prefactor  $\varsigma$ .

$$\frac{U_{Zeeman}}{k_B T} = \frac{-\mu_0 M_s^2}{4\pi k_B T} \left( \frac{\pi d_m^3}{6} \right)^2 \left( \frac{1 \text{ grid unit}}{d_{phys}} \right)^3 \left[ \frac{3(\hat{m}_s \cdot \hat{r}) - 1}{|\vec{r}|^3} \right] \quad (5)$$

$$\varsigma = \frac{\mu_0 M_s^2}{4\pi k_B T} \left( \frac{\pi d_m^3}{6} \right)^2 \left( \frac{1 \text{ grid unit}}{d_{phys}} \right)^3 \quad (6)$$

Suppose that an ensemble of particles is built up one by one, with particles remaining permanently bound to the sites where they are added. These particles could be added randomly to available sites, as in the example shown in Figure 4B. Alternatively, the pseudorandom addition of particles can be weighted according to a scheme motivated by statistical mechanics in order to take into account the influence of magnetic interaction compared to thermal fluctuation. The total energy of a test dipole at any grid site  $U_{i,j}$  is just a sum of the dipole interactions with all the particles presently on the grid. If the weighting scheme assumed for the addition of particles follows a Maxwell distribution, then the probability of adding a new particle to an available site  $p_{i,j}$  is given by:

$$p_{i,j} = \frac{\exp\left(-\frac{U_{i,j}}{k_B T}\right)}{Q} \quad (7)$$

Where  $Q$  is the partition function.

$$Q = \sum_{i,j}^{all \text{ available } i,j} \exp\left(-\frac{U_{i,j}}{k_B T}\right) \quad (8)$$

Figures 4B, D, and F show that the energy of magnetic interaction predicted for sites close to particles on the grid is attractive and of comparable or larger magnitude to the ambient thermal energy. (I.e., for sites close to particles,  $U_{i,j}/k_B T \leq -1$ ).

One additional aspect of the model worth consideration is the influence of the particles upon the orientation of the moments of their neighbors. Neighbors will exert torques upon each other and thereby influence the overall profile of the magnetic field. In a real system, one can imagine that the orientation of moments would fluctuate, but exhibit correlation with the local field. Rather than account for this complexity directly, we instead considered two comparatively simple extreme cases: randomized moments with no correlation and fully correlated moments.

In order to consider the second case, an algorithm was employed that begins by randomly sampling different moment orientations to coarsely determine a minimal energy configuration. After this, the moments are finely relaxed into alignment with the local field. Both the uncorrelated and fully correlated cases lead to clustering when magnetic interactions are taken into account, as shown in Figures 4D and F. Assuming interaction with uncorrelated and randomized moments, a single cluster was typically formed, and hence a lower median interparticle distance was predicted (Figures 4C, D). In the case of fully correlated moments, the tendency is to form chains, demonstrated quantitatively by comparing the distance of each particle from the line defined by the two particles previously added, or “chain departure distance” (Figures 4E, F). That these chains tend to form horizontally and vertically is likely a numerical artifact, a consequence of the fact that the mesh is rectangular and the distance between grid points is minimal in these directions. The correlated moments often form multiple clusters because the superposition of dipole fields from a chain of aligned dipoles results in large magnitudes at the ends, and comparatively small magnitudes near the middle of the chain. This, in combination with the possibility that a site at the end of an existing chain



might be unavailable for binding, provides an explanation for the frequent occurrence of multiple clusters in the simulations with correlated moments.

It should be emphasized that this model is highly simplified in order to illustrate that magnetic interaction could plausibly account for clustering behavior of ideally superparamagnetic particles as they bind to A $\beta$ , even though they are stably suspended in solution. Though relevant features are physically motivated, it is not intended as a fully rigorous model. For instance, the presence of binding sites would be determined by protein structure, rather than assuming the whole A $\beta$  surface is available. Binding would not necessarily be permanent, and it would be more rigorous to consider the spatial variation of the full free energy governing the behavior of the particles in solution. Despite their spherical appearance, the particles would exhibit magnetic anisotropy, whether arising primarily from the cubic magnetocrystalline anisotropy of magnetite or from subtle eccentricity in their shape. In a more computationally intensive treatment, perhaps particles could be modeled as undergoing a 3D weighted random walk in solution, with each step influenced by their interaction with a spatially variable 3D free energy determined by the solution and the A $\beta$  fibrils. Despite its simplifications, the approach that we implemented offers predictions that are in good qualitative agreement with TEM data and clarifies the expected effect of magnetic interaction on binding.

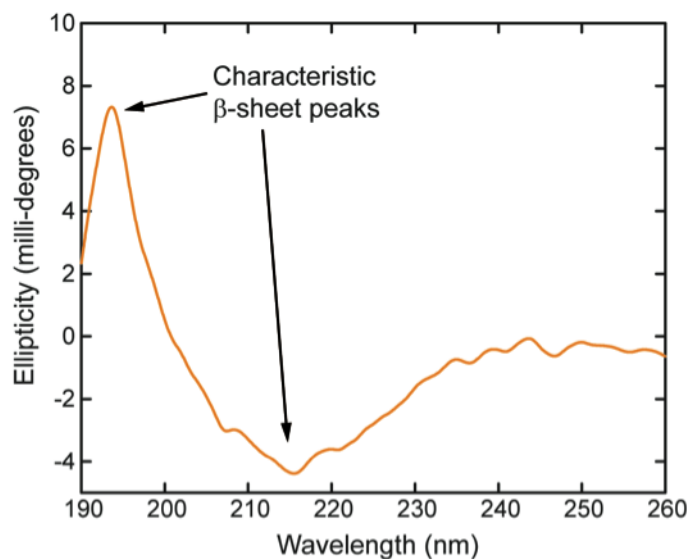
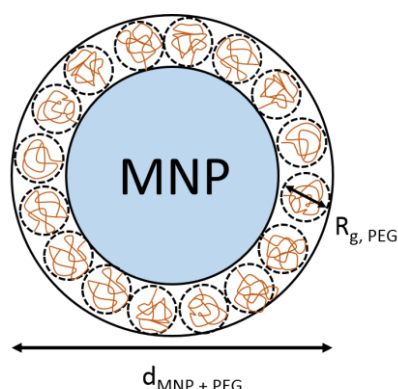


**Figure S1.** To confirm the aggregation state of A $\beta$ , an Aviv Model 202 CD spectrometer was used to probe the secondary structure of A $\beta$ . The amyloid sample was aggregated at physiological conditions for 168 hrs and was placed in a 1 mm pathlength quartz cuvette (Hellma cells) for CD analysis. We conclude from the CD data that the amyloid sample has a characteristic  $\beta$ -sheet conformation consistent with literature, exhibited by the positive peak around 196 nm and negative peak around 217 nm.<sup>[61]</sup>



Estimated number of conjugated ligands	PEG 10 kDa	LPFFD
Lower bound	50% (conversion efficiency): 75	20%: 15
Upper bound	80%: 120	50%: 60
Theoretical upper limit	100%: 150	100%: 150

**Figure S2.** Schematic illustration of the proposed close-packed structure of PEG chains on MNP surface. The number of 10 kDa PEG ligands conjugated to the surface of 22 nm MNPs is limited by the size of the polymer. To estimate the number of ligands that could theoretically be packed on the MNP surface, we first took into account the radius of gyration ( $R_g$ ) of 10 kDa PEG, which was estimated from Linegar et al.:  $R_g = 0.0215M_w^{0.583 \pm 0.031}$  to be 4.6 nm.<sup>[62]</sup> The number of PEG chains in the close-packed structure was calculated using:

$$N_{PEG} = \frac{V_{MNP+PEG} - V_{MNP}}{V_{PEG}} * 0.74, \text{ where } V \text{ is volume and } 0.74 \text{ is the atomic packing factor for}$$

a close-packed structure. The theoretical upper limit of PEG chains that could be conjugated to available carboxyl groups on the MNP surface is 150 PEG chains. We estimated 50-80% conversion efficiency for the first NHS/EDC coupling reaction of PEG to MNPs and 20-50% conversion efficiency for the second NHS/EDC coupling reaction of LPFFD to PEG.

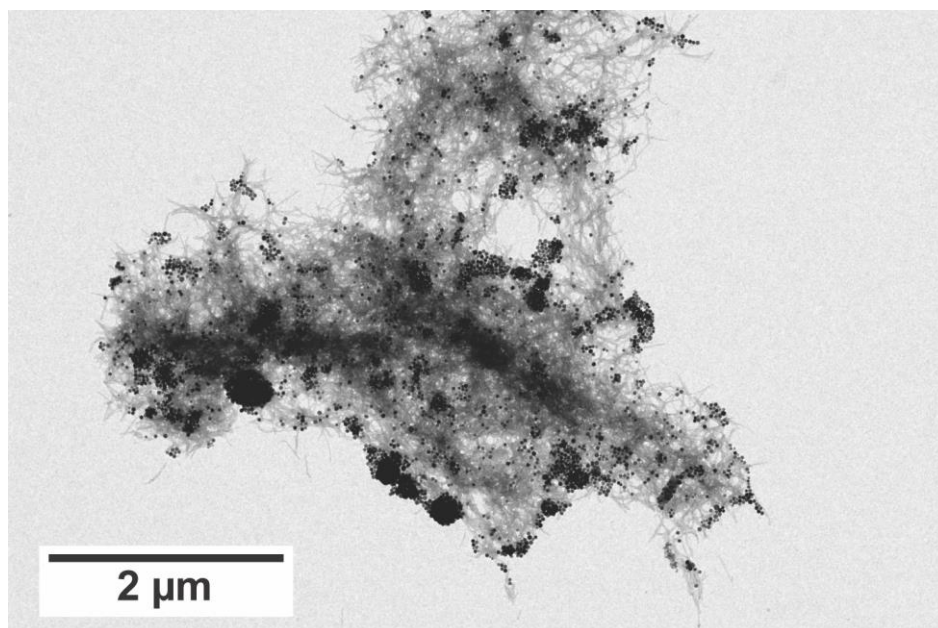


**Figure S3.** TEM image of A $\beta$  with MNP-PEG-LPFFD. MNPs are non-uniformly bound to amyloid fibrils, which motivated the development of the simulation in Figure 4. MNPs form big clusters, small chains, and some smaller clusters on the A $\beta$  backbone. This behavior is consistent with the statistical model for the distribution of interacting magnetic dipoles.

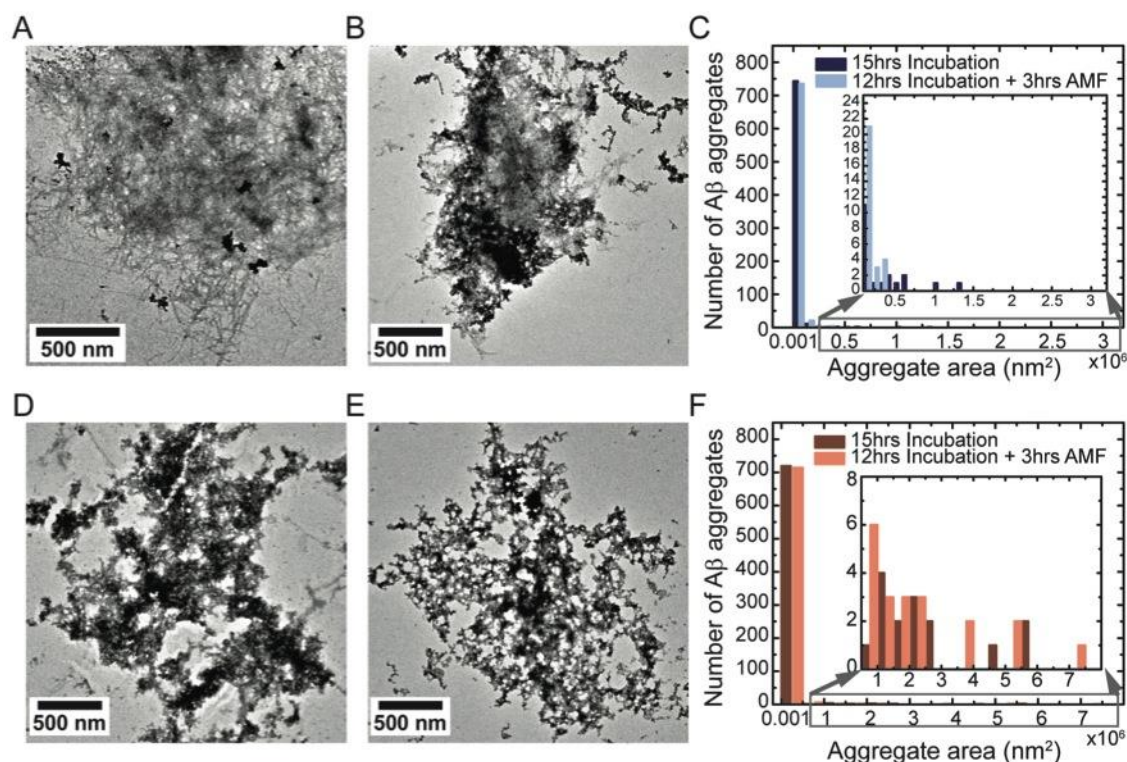


**Figure S4.** TEM images and size distribution image analysis for controls of 12-hr-old A $\beta$  samples ( $n = 10$ ). Representative TEM images of A $\beta$  aggregates (A) untreated and (B) treated with 3 hrs of AMF. (C) Image analysis of size distribution of A $\beta$  aggregates untreated and treated with 3 hrs AMF. Since both distributions are not normally distributed (two-sample Kolmogorov-Smirnov test) we performed a two-sided Wilcoxon rank-sum test, which did not show statistical difference ( $p = 0.6126$ ). Therefore AMF exposure to A $\beta$  alone does not have a significant effect on aggregate size. Representative TEM images of A $\beta$  aggregates in presence of MNP-PEG (D) untreated and (E) treated with 3 hrs of AMF. (F) Image analysis of size distribution of A $\beta$  aggregates in presence of MNP-PEG untreated and treated with 3hrs AMF. Both distributions are not statistically different (two-sided Wilcoxon rank-sum test,  $p = 0.4904$ ). Therefore AMF exposure to A $\beta$  + NP-PEG does not have a significant effect on aggregate size.

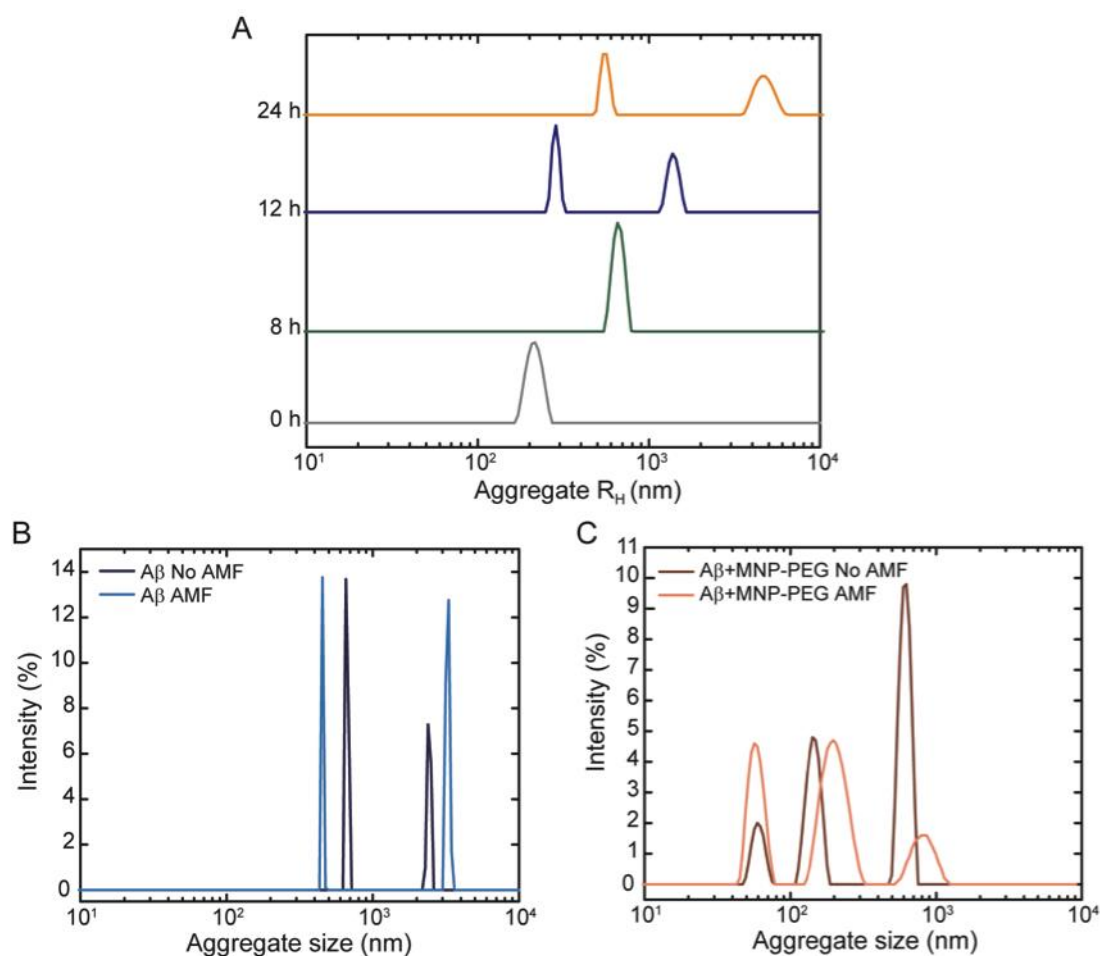


**Figure S5.** (A) DLS size distribution of A $\beta$  at 0, 8, 12 and 24 hrs of incubation at physiological conditions. (B) DLS size distribution of 12 hr-old A $\beta$  sample with and without exposure to 3 hrs AMF. (C) 12hr-old A $\beta$  decorated with MNP-PEG with and without AMF exposure. A significant change in hydrodynamic radius is not observed for control samples of A $\beta$  alone or A $\beta$  in the presence of PEG-MNPs after AMF exposure.

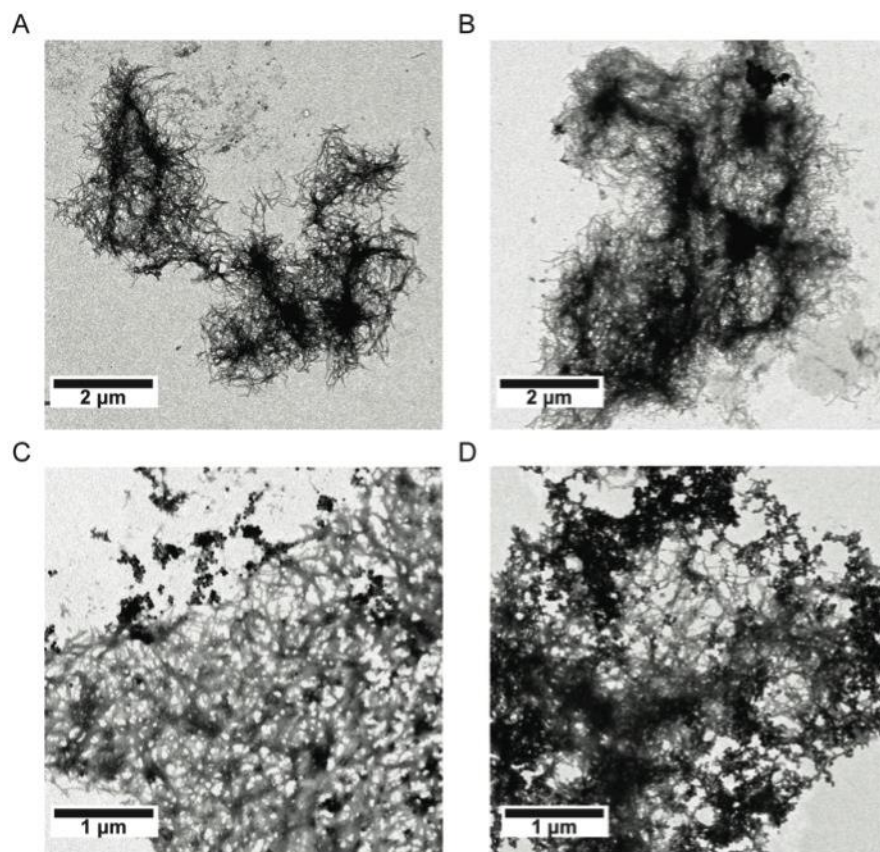


**Figure S6.** TEM controls of 168-hr-old sample. Representative TEM images of A $\beta$  aggregates (A) untreated and (B) treated with 6 hrs of AMF. Representative TEM images of A $\beta$  aggregates in presence of MNP-PEG, (C) untreated and (D) treated with 3 hrs of AMF.



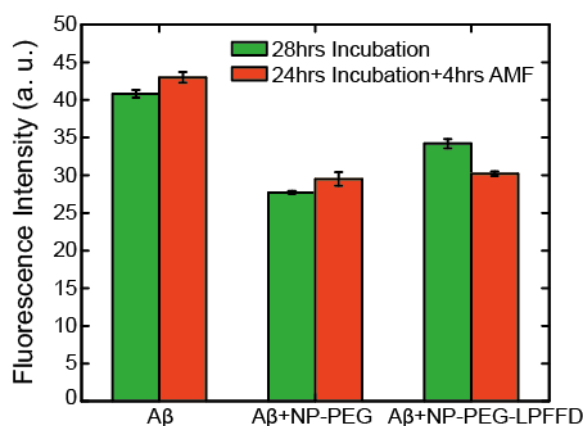


**Figure S7.** Fluorescence intensity of 24-hr-old A $\beta$  AMF-treated (orange) and untreated (green) samples. Using ThT, a particular aggregation state can be linked with fluorescence intensity. For the A $\beta$  sample with no MNPs, a small increase in fluorescence is exhibited after the AMF test due to accelerated aggregation that occurs at elevated temperatures during the course of the experiment. (Fluctuations of  $\pm 2$  °C occur in our apparatus). For the A $\beta$  sample with non-targeted MNPs, the fluorescence does not dramatically change. The natural tendency for the A $\beta$  would be to continue aggregating over time and exhibit an increase in fluorescence during the AMF test. However, some of the MNPs become nonspecifically trapped in the aggregate structure and upon AMF stimulation, we hypothesize that the local heating of the MNPs causes A $\beta$  aggregate fragmentation. The sample with targeted MNPs exhibits an overall decrease in fluorescence following AMF stimulation. This correlates with the disruption of  $\beta$ -sheet structure (hydrophobic interactions and hydrogen bonds) by the local heating of targeted MNPs.



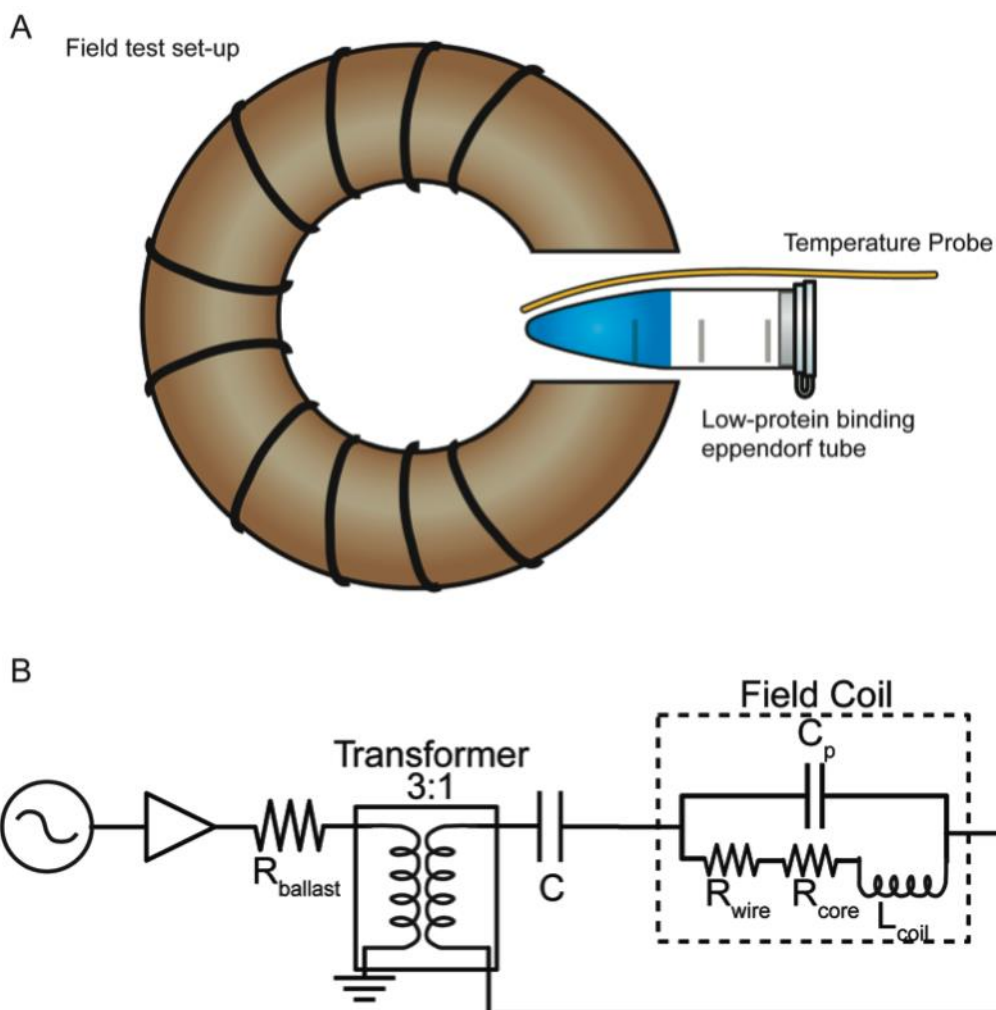


**Figure S8.** Experimental field test and magnetic coil set-up. (A) A magnetic field was applied by inserting the sample into the gap of a custom-built coil with a soft ferromagnetic core (B) driven by an RLC resonance circuit.

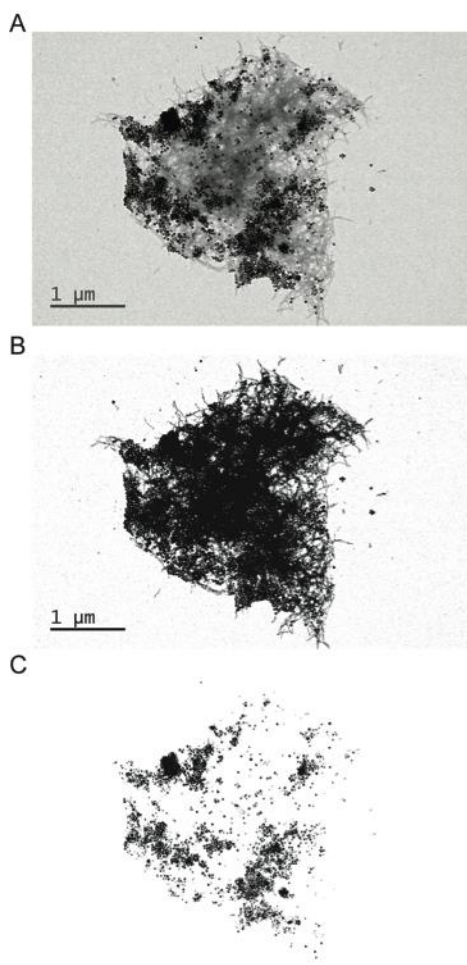


**Figure S9.** TEM image processing and thresholding method using Image J<sup>[59]</sup> for targeting analysis. (A) Original TEM image. (B) Threshold to remove background; fibrils and MNPs remaining. (C) Threshold to remove background and fibrils; only MNPs remaining.

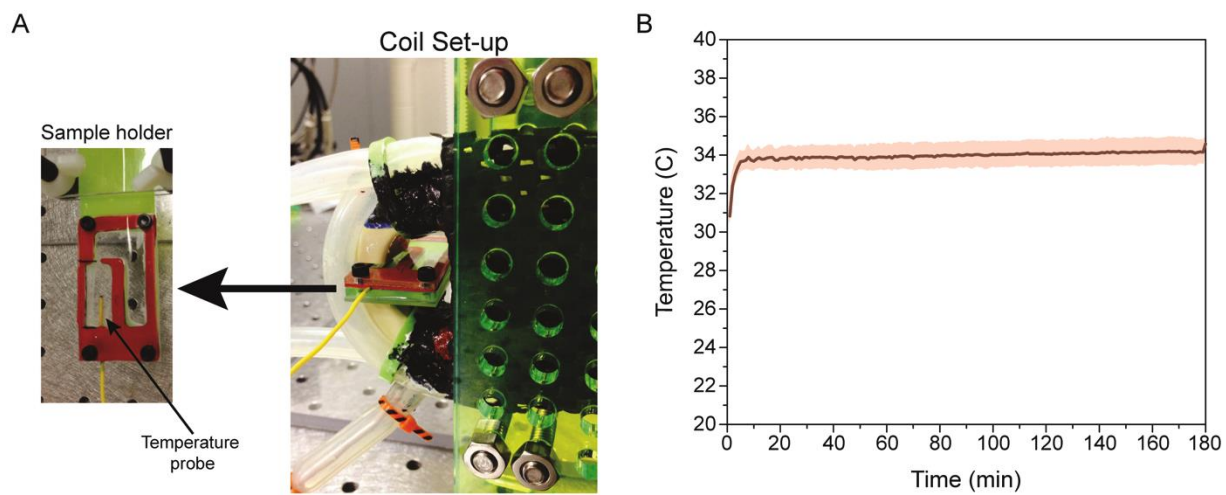


**Figure S10.** Cell viability AMF experimental set-up. (A) Photo of the coil set-up used for cell viability experiments. Inset photo of the sample holder for neurons. (B) Temperature profile during 3h AMF treatment of hippocampal neurons.